AD-A111 452   NAVAL RESEARCH LAB WASHINGTON DC   F/G 4/1
IONOSPHERIC IRREGULARITY PHYSICS MODELLING.(U)
FEB 82   S L OSSAKOW, M J KESKINEN, S T ZALESAK
UNCLASSIFIED   NRL-MR-4741   NL

END
DATE
FILMED
-82
DTIC

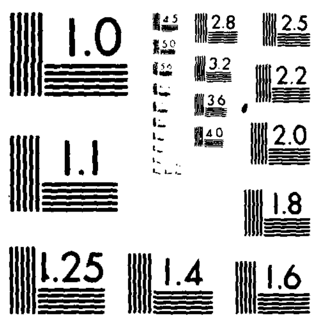

MICROCOPY RESOLUTION TEST CHART
NATIONAL BUREAU OF STANDARDS 1963 A

Ionospheric Irregularity Physics Modelling

S. L. Ossakow, M. J. Keskinen, and S. T. Zalesak

Geophysical and Plasma Dynamics Branch
Plasma Physics Division

February 9, 1982

This research was sponsored by the Defense Nuclear Agency under Subtask S99QAXHC, work unit 00032 and work unit title "Plasma Structure Evolution."

NAVAL RESEARCH LABORATORY
Washington, D.C.

SECURITY CLASSIFICATION OF THIS PAGE (When Data Entered)

REPORT DOCUMENTATION PAGE		READ INSTRUCTIONS BEFORE COMPLETING FORM
1. REPORT NUMBER: NRL Memorandum Report 4741	2. GOVT ACCESSION NO.: AD-A111 452	3. RECIPIENT'S CATALOG NUMBER
4. TITLE (and Subtitle): IONOSPHERIC IRREGULARITY PHYSICS MODELLING*		5. TYPE OF REPORT & PERIOD COVERED: Interim report on a continuing NRL problem.
		6. PERFORMING ORG. REPORT NUMBER
7. AUTHOR(s): S. L. Ossakow, M. J. Keskinen, and S. T. Zalesak		8. CONTRACT OR GRANT NUMBER(s)
9. PERFORMING ORGANIZATION NAME AND ADDRESS: Naval Research Laboratory, Washington, DC 20375		10. PROGRAM ELEMENT, PROJECT, TASK AREA & WORK UNIT NUMBERS: 62715H; 47-0889-0-2
11. CONTROLLING OFFICE NAME AND ADDRESS: Defense Nuclear Agency, Washington, DC 20305		12. REPORT DATE: February 9, 1982
		13. NUMBER OF PAGES: 52
14. MONITORING AGENCY NAME & ADDRESS (if different from Controlling Office)		15. SECURITY CLASS. (of this report): UNCLASSIFIED
		15a. DECLASSIFICATION/DOWNGRADING SCHEDULE

16. DISTRIBUTION STATEMENT (of this Report)

Approved for public release; distribution unlimited.

17. DISTRIBUTION STATEMENT (of the abstract entered in Block 20, if different from Report)

18. SUPPLEMENTARY NOTES

This research was sponsored by the Defense Nuclear Agency under Subtask S99QAXHC, work unit 00032, and work unit title "Plasma Structure Evolution."

*This is based on talk presented at AIAA 20th Aerospace Sciences Conference, 11—14 January 1982, Orlando, Florida.

19. KEY WORDS (Continue on reverse side if necessary and identify by block number)

Ionospheric irregularities
Physics modelling
Plasma cloud striations
Equatorial spread F phenomena
High latitude diffuse auroral irregularities
Nonlinear simulations

20. ABSTRACT (Continue on reverse side if necessary and identify by block number)

Theoretical and numerical simulation techniques have been employed to study ionospheric F region plasma cloud striation phenomena, equatorial spread F phenomena, and high latitude diffuse auroral F region irregularity phenomena. Each of these phenomena can cause scintillation effects. The results and ideas from these studies are state-of-the-art, agree well with experimental observations, and have induced experimentalists to look for theoretically predicted results. One conclusion that can be drawn from these studies is that ionospheric irregularity phenomena can be modelled from a first principles physics point of view. Theoretical and numerical simulation results from the aforementioned ionospheric irregularity areas will be presented.

DD FORM 1 JAN 73 1473 EDITION OF 1 NOV 65 IS OBSOLETE
S/N 0102-014-6601

SECURITY CLASSIFICATION OF THIS PAGE (When Data Entered)

CONTENTS

IONOSPHERIC IRREGULARITY PHYSICS MODELLING

I. Introduction

The term ionospheric irregularities has become synonymous with the terms plasma (or electron) density fluctuations, structure, and striations. Under a wide variety of different conditions, ionospheric irregularities are exhibited at all geomagnetic latitudes, longitudes, and almost all altitudes. These irregularities are generally magnetic field aligned, i.e., there is hardly any variation along the geomagnetic field. Thus, the irregularity wavelength perpendicular to the geomagnetic field is much smaller than its parallel wavelength. The two dimensional nature of the irregularities means that detailed two dimensional (perpendicular to the ambient magnetic field) numerical simulations can be performed. There is a diversity of scale sizes associated with ionospheric irregularities, spanning some 5-6 orders of magnitude (10's of centimeters to many kilometers). While this diversity makes for a richness of study, numerical simulations, with todays computer storage, etc., cannot possibly handle this broad scale spectrum, i.e., the problem must be examined in pieces. Nevertheless, the inadequacy of linear instability theories to describe most aspects of ionospheric irregularities and their attendant effects has led to studying from a first principles physics point of view, by theoretical and numerical simulation techniques, the nonlinear evolution of the various irregularities. The study of ionospheric irregularities requires: (i) a description of the zeroth order (laminar or mean flow) state of the ionosphere; (ii) a relevant instability mechanism; and (iii) the ability to follow the nonlinear development of such instabilities.

The practical importance of such studies of ionospheric irregularities derives primarily from the fact that such irregularities can degrade satellite C^3I systems through scintillation effects (e.g., for the case of F region irregularities, irregularities with wavelengths $\sim$ 100's of meters to $\sim$ kilometer can cause scintillation effects). The studies should be able to provide a predictive capability in terms of where these irregular structures can be expected and what their properties will be.

This paper presents an overview of studies carried out, using theoretical and numerical simulation techniques, for ionospheric F region

Manuscript submitted December 4, 1981.

irregularities caused by plasma instabilities. Results will be presented from studying: (A) ionospheric F region plasma cloud striation phenomena (generated by the $\underline{E} \times \underline{B}$ gradient drift instability); (B) equatorial spread F phenomena (generated by the collisional Rayleigh-Taylor instability); and (C) high latitude diffuse auroral F region irregularity phenomena (generated by the current convective instability and $\underline{E} \times \underline{B}$ gradient drift instability). For further study the interested reader is referred to references 1-4 for recent reviews of the field.

II. Theory

Initially, we will be interested in long wavelengths (i.e., much greater than the ion gyroradius). Thus, the starting point is the basic plasma fluid equations, which will be applicable to all the ionospheric F region irregularity phenomena which we present. When we study the individual irregularity phenomena stated in section I, we will make the appropriate approximations. The two fluid equations which describe the electron and ion dynamics are as follows.

$$\frac{\partial n_\alpha}{\partial t} + \nabla \cdot (n_\alpha \underline{V}_\alpha) = P - \nu_R n_\alpha \tag{1}$$

$$m_\alpha n_\alpha \left(\frac{\partial}{\partial t} + \underline{V}_\alpha \cdot \nabla\right)\underline{V}_\alpha = -\nabla p_\alpha + e_\alpha n_\alpha \left(\underline{E} + \frac{\underline{V}_\alpha x \underline{B}}{C}\right)$$

$$+ m_\alpha n_\alpha (\underline{g} - \nu_{\alpha n}(\underline{V}_\alpha - \underline{U})) - \underline{R}_\alpha \tag{2}$$

$$\underline{R}_e = -\underline{R}_i = m_e n_e \nu_{ei} (\underline{V}_e - \underline{V}_i) \tag{3}$$

$$\nabla \cdot \underline{J} = 0 \tag{4}$$

$$\underline{J} = \Sigma\, n_\alpha e_\alpha \underline{V}_\alpha \tag{5}$$

In the above equations the subscript α denotes species (subscript e is electron, i is ion), n is density, $\underline{V}$ is fluid velocity, P is production, ν_R is the chemical recombination coefficient, p is the scalar pressure (p = nT, T expressed in energy units), ∇ is the gradient operator, $\underline{B}$ is the ambient magnetic field (taken to be uniform), e_α is the charge, c is the speed of light, m is mass, $\underline{g}$ is gravity, $\nu_{\alpha n}$ is the charged particle-neutral collision frequency, $\underline{E}$ is electric field, $\underline{U}$ is neutral wind velocity, ν_{ei} is the Coulomb collision frequency, and $\underline{J}$ is current. Equation (4) can be obtained from (1) by using the appropriate form of (1) for electrons and ions, subtracting the two equations and setting $n_e \approx n_i \approx n$. Equation (1) is the continuity equation, (2) is the momentum equation, and (4) is the divergence of the current.

We briefly outline the mathematical representations (solution methods) that are involved and basically common to all three processes (plasma cloud striations, equatorial spread F, and high latitude diffuse auroral F region irregularities). We use numerical simulations of the appropriate system of coupled nonlinear differential equations which are derived theoretically and thought to represent the process being studied (variations of (1)-(5)). Starting with the three dimensional continuity and momentum equations for the ions and electrons (1), we note that the spatial and temporal scales of physical interest are as such to allow us to make the following simplifications. The electric field is electrostatic and thus representable by $E = -\nabla\phi$. The geometry is basically two-dimensional, i.e., the negligible components of $\nabla\phi$ and the ion velocity parallel to $\underline{B}$ allow us to reduce the 3D problem to a series of 2D problems coupled by the invariance (or near invariance) of ϕ along a field line (to be sure for the high latitude diffuse auroral irregularities with the current convective instability special care must be taken). Quasi-neutrality holds, i.e., $n_e \approx n_i$ and results in (4). After making the above simplifications and neglecting inertial effects we are left with two general types of two dimensional partial differential equations: (a) one or more nonlinear continuity equations for ions or electrons (hyperbolic, initial boundary value) and (b) a single linear equation for the electrostatic potential ϕ (elliptic, boundary value, large sparse matrix) which is a Poisson-like equation resulting from $\nabla \cdot \underline{J} = 0$.

III. Examples of Ionospheric Irregularities Studied

A. Plasma Cloud Striations

Experimental studies[5-7] of artificially injected plasma clouds into the ionosphere have provided a great amount of information concerning not only ambient ionospheric conditions, e.g., electric and magnetic fields, but also the structure and morphology of evolving plasma clouds themselves by means of, for example, scintillation and power spectrum studies. The characteristic plasma cloud initial steepening, elongation, and striation formation have been explained by applying the linear theory of the $\underline{E} \times \underline{B}$ gradient drift instability, originally developed for laboratory plasmas[8], to plasma cloud geometries.[9-12] More recently the nonlinear stabilization of the long wavelength $\underline{E} \times \underline{B}$ gradient drift instability in ionospheric plasma clouds has been studied.[13] Numerical simulation studies[14-21] of barium plasma clouds with a background ionosphere have reproduced not only many of the gross observational features of plasma cloud evolution, but also their spatial power spectra[22], minimum scale size[23-24] and outer scale size or correlation length.[25] Furthermore, numerical simulations of the local $\underline{E} \times \underline{B}$ gradient drift instability in ionospheric plasma clouds[26] have yielded spatial power spectra and saturated wave amplitudes that are consistent with experiment.

Figure 1 depicts the basic $\underline{E} \times \underline{B}$ gradient drift instability geometry for studying plasma cloud striations. We are showing a simplified one dimensional geometry for the initial plasma cloud density profile (or Pedersen conductivity), N(y). In reality the cloud is initially two dimensional perpendicular to the ambient magnetic field, $\underline{B}$. However, for simplicity and the fact that the initial one dimensional cloud geometry develops two dimensional ($\perp \underline{B}$) structure (striations) similar to the initial 2D cloud, we have chosen to use, in figures 1 and 2, an initial 1D plasma cloud. In figure 1 the electric field, $\underline{E}$, is in the x direction so that $\underline{E} \times \underline{B}$ is in the negative y direction and the so-called back side of the cloud is on the positive y side. This striation geometry is equivalent to having a neutral wind, $\underline{U}$, blowing in the y direction and having no $\underline{E}$. In figure 1 k represents a perturbation vector.

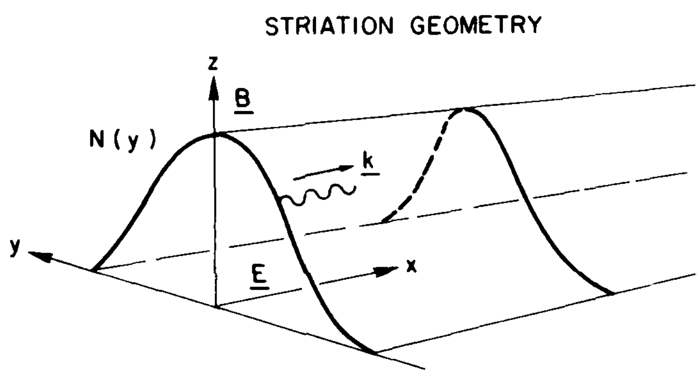

Fig. 1 — Simplified $\underline{E} \times \underline{B}$ striation geometry

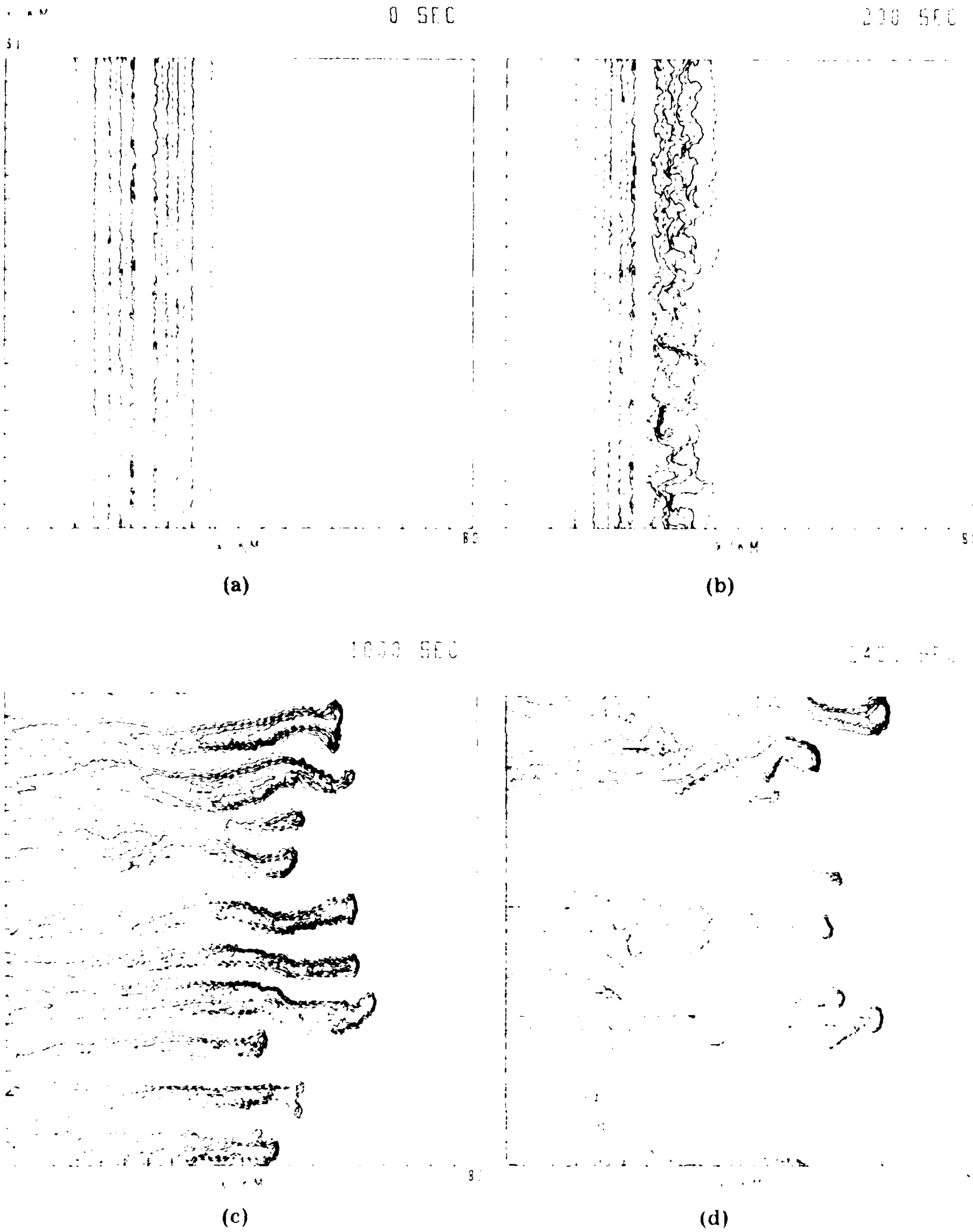

Fig. 2 — Real space isodensity contour plots of $\Sigma(x,y)/\Sigma_0$ for L = 6 km using the 3% random initial conditions at (a) t = 0 sec, (b) t = 200 sec, (c) t = 1000 sec, and (d) t = 2400 sec (after ref. 20).

For barium clouds released at 200 km or more $\nu_\alpha/\Omega_\alpha \ll 1$, where $\Omega_\alpha \equiv (e_\alpha B/m_\alpha c)$. The electrical conductivity of the plasma is dominated by the Pedersen conductivity, $\sigma_p \approx (nec/B)(\nu_{in}/\Omega_i)$. Due to the very high conductivity, $\sigma_\parallel$, along magnetic field lines (typically $\sigma_\parallel/\sigma_p \sim 10^6$), the magnetic field lines may be regarded as equipotentials and, as a result, a field line integrated (2D) model is justified.[11-12] Furthermore, for large plasma clouds (i.e., large magnetic field line integrated Pedersen conductivity compared with that of the background ionosphere) the cloud interaction with the background level (second level, i.e., a separate continuity equation and momentum equation for ionospheric ions) is ignored[11,14,21,23-24]. Thus, using an x,y,z coordinate system with $\underline{B} = B\hat{\underline{z}}$ (B also uniform), ambient electric field $E_o\hat{\underline{y}}$ and after transforming to a frame drifting with the $\underline{E}_o \times \underline{B}$ velocity, $\underline{V}_o = (cE_o/B)\ \hat{\underline{x}}$ the 2D model equations for the magnetic field line integrated plasma cloud Pedersen conductivity Σ (x,y) (where $\Sigma(x,y) = \int \sigma_p dz$) and the self-consistent plasma cloud electrostatic potential $\hat{\phi}$, the set of equations (1)-(5)) can be written as[12,21,23-24]

$$\frac{\partial \Sigma}{\partial t} + \frac{c}{B}\,(\hat{\underline{z}} \times \nabla\hat{\phi})\cdot\nabla\Sigma = D\nabla^2\Sigma \tag{6}$$

$$\nabla\cdot(\Sigma\nabla\hat{\phi}) = \underline{E}_o\cdot\nabla\Sigma \tag{7}$$

$$D = 2T\,\frac{(\nu_{ei}+\nu_{en})}{ceB\Omega_e} \tag{8}$$

where $\nabla\hat{\phi} = \underline{E}_o - \underline{E}(x,y)$, $\underline{E}(x,y)$ is the total electrostatic field, $\nabla \equiv (\partial/\partial x,\ \partial/\partial y)$, and D is the cross field diffusion coefficient. For barium plasma clouds D lies in the range 0.6 - 6 m^2/s. Equation (6) results from the magnetic field-line integration of the ion continuity equation while (7) is derived from the current conservation, (4). Also in obtaining (6) and (7) the neutral wind has been set to zero. If we set D = 0 then we have the simplest set of equations describing striation phenomena in F region ionospheric plasma clouds.

By linearizing (6) and (7) i.e., $\Sigma = \Sigma_o + \hat{\Sigma}$, etc., and

assuming $\hat{\Sigma}$, $\hat{\phi} \propto \exp[i(k_y y + k_x x - \omega t)]$ with $\underline{k} \cdot \underline{B} = 0$, $kL \gg 1$ we find the usual $\underline{E} \times \underline{B}$ gradient drift instability growth rate

$$\gamma = \frac{cE_o}{BL} \left(\frac{k_y}{k}\right)^2 - Dk^2 \tag{9}$$

where $k^2 = k_x^2 + k_y^2$, $\omega \equiv \omega_r + i\gamma$, $L^{-1} = \partial \ \ln \Sigma_o/\partial x$. Equation (9) shows that only one side of the plasma cloud is unstable (positive L).

Numerical Simulations. Equations (6) and (7) were solved numerically on a mesh consisting of 258 grid points in the x direction ($\underline{E}_o \times \underline{B}$ direction) and 102 points in the y direction. With a constant grid spacing of 310 meters, the real space dimensions of the mesh were 80 km along x and 31 km along y. The magnetic field line integrated Pedersen conductivity $\Sigma(x,y)$ in (6) was advanced in time using a multi-dimensional flux-corrected variable time step leapfrog-trapezoid scheme[27] which is second order in time and fourth order in space. At each timestep the self-consistent electrostatic potential $\hat{\phi}$ due to the ion cloud was determined from (7) using a Chebychev iterative method[28,29] with a convergence criterion of 10^{-4}. Periodic boundary conditions were imposed along the y direction with Neumann conditions ($\partial/\partial x = 0$) along the x direction. These boundary conditions result in a realistic representation of plasma inflow-outflow at the boundaries in the $\underline{E}_o \times \underline{B}$ direction.

Initially, the field line integrated Pedersen conductivity of the plasma cloud was taken to be of the form

$$\Sigma(x,y,t=0)/\Sigma_o = [M \exp(-x^2/L^2) + 0.1](1 + \varepsilon(x,y)) \tag{10}$$

Numerical studies have been done where $\varepsilon(x,y)$ was given an rms value of 3% and generated from a randomly phased Gaussian power spectrum[23-25]. Also, two other cases have been studied[30]: in one case $\varepsilon(x,y) = A \cos 3k_F y$, a single monochromatic wave along the linearly most unstable y direction with wavelength $\lambda = 2\pi/3k_F = 10$ km where $k_F = 2\pi/30$ km^{-1} and the other case $\varepsilon(x,y) = A(1-2r(x,y))$ where $r(x,y)$ is a random number between 0 and 1. The second case models the many wave initial condition (it produces an $\varepsilon(k)$ which is essentially flat in k space) and it is this one which we

present here.

Figures 2a–2d illustrate the evolution of an initially slab-like barium plasma cloud driven unstable by using purely random initial conditions with maximum amplitude of 3% (A = 0.03) for L = 6 km (Reference 30 also presents an A = 0.15). Also for this simulation V_o = 100 m/s, D = 1m^2/s, and M (in eqn. (10)) = 1, so that the maximum ratio of the field line integrated cloud Pedersen conductivity to the background ionosphere is approximately 10. In this simulation the initial evolution of a test wave is influenced not only by the ambient plasma cloud, but also by a many wave background. Figure 2b displays the cloud at t = 200 sec and shows the initial random perturbations developing on the backside. Figure 2c shows the field line integrated Pedersen conductivity contours at t = 1000 sec with striation development and elongation in evidence. Figure 2d shows the cloud configuration at t = 2400 sec and is similar to the late time configurations using other[30] initial perturbation conditions.

Figure 3 shows sample 1D power spectra of plasma cloud Pedersen conductivity both parallel $P(k_x)$ and perpendicular $P(k_y)$ to the $\underline{E}_o \times \underline{B}$ drift corresponding to t = 2400 sec of figure 2. These power spectra were obtained by first Fourier transforming the real space cloud Pedersen conductivity $\delta\Sigma(x,y) \rightarrow \delta\Sigma(k_x, k_y)$ where $\delta\Sigma(x,y) = \Sigma(x,y)-\Sigma_o$, Σ_o the maximum cloud conductivity. The power spectral density $|\delta\Sigma(k_x,k_y)/\Sigma_o|^2$ was then formed and the one-dimensional power spectra $P(k_x)$and $P(k_y)$ were computed where

$$P(k_x) = \int dk_y |\delta\Sigma(k_x,k_y)/\Sigma_o|^2 \qquad (11)$$

and

$$P(k_y) = \int dk_x |\delta\Sigma(k_x,k_y)/\Sigma_o|^2 \qquad (12)$$

These transverse averaged power spectra $P(k_x)$ and $P(k_y)$ were then fitted[25] with a three parameter (spectral strength $P_{o\alpha}$, spectral index n_α and outer scale wavenumber $k_{o\alpha}$) power law of the form

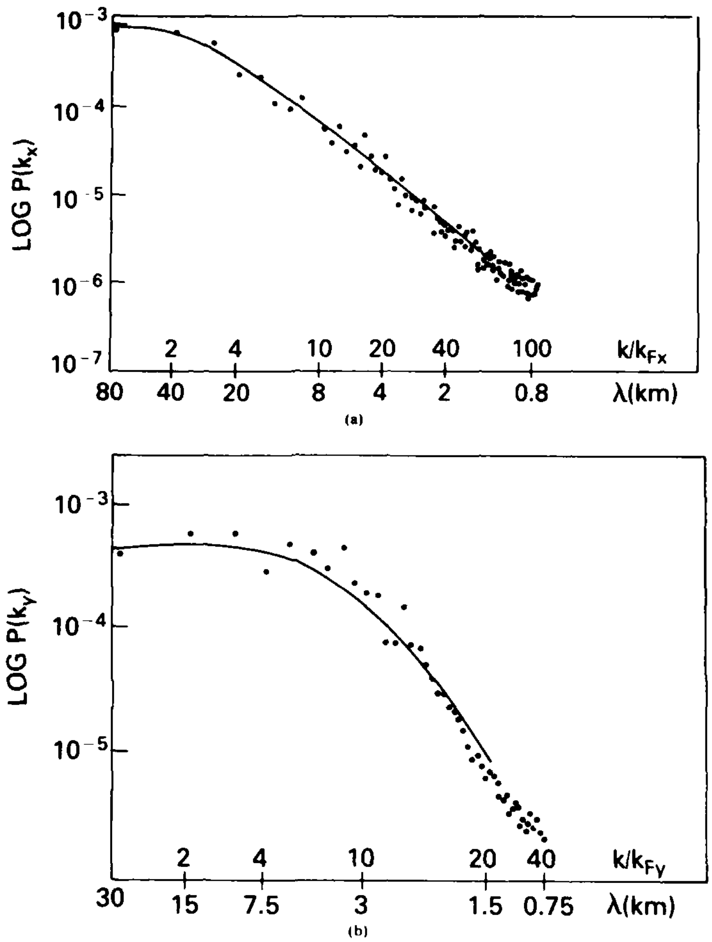

Fig. 3 — One dimensional (a) x power spectrum $P(k_x)$ and (b) y power spectrum $P(k_y)$ at t = 2400 sec for L = 6 km using the 3% random initial conditions with n_x=2, $2\pi/k_{ox}$ = 32 km, and n_y=2.4, $2\pi/k_{oy}$ =3.8 km (after ref. 30).

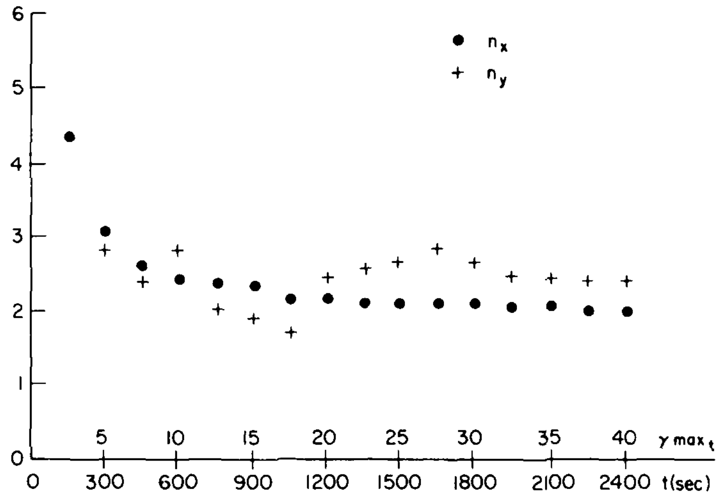

Fig. 4 — Time history of best fit spectral indices n_x and n_y for L = 6 km using the 3% random initial conditions (after ref. 30)

$$P(k_\alpha) = P_{o\alpha}(1 + k_\alpha/k_{o\alpha})^{-n_\alpha/2} \tag{13}$$

where α = x or y. The method used to extract the best fit parameters $P_{o\alpha}$, n_α, $k_{o\alpha}$ is a nonlinear least squares procedure[25] which computes $P_{o\alpha}$ and n_α directly and then iterates to find $k_{o\alpha}$. The time histories of the best fit spectral indices n_x and n_y are displayed in figure 4. After initial transients, the spectral index in the $\underline{E}_o \times \underline{B}$ direction becomes $n_x \approx 2$ with $n_y \approx 2\text{-}3$. These spectral indices are in agreement with both experimental values[7,31] and previous one level[24,25] and two level[22] numerical simulations of ionospheric barium clouds using different initial conditions.

Summary. Plasma fluid equations have been used to study, by numerical simulation methods, the nonlinear evolution of plasma cloud striation phenomena, where the striations are driven by the $\underline{E} \times \underline{B}$ gradient drift instability. The one dimensional power spectra shown in figures 3 and 4 exhibit a power law spectrum, i.e., the x power spectrum is $\propto k_x^{-n_x}$ with $n_x \approx 2$ for $2\pi/k_x$ between 1 and 80 km, while the y spectrum $\propto k_y^{-n_y}$ with $n_y \approx 2\text{-}3$ for $2\pi/k_y$ between 1 and 10 km. The numerical results are consistent with recent experimental[7,31], theoretical[13,32] and other numerical simulation[25,26] studies of ionospheric plasma clouds (reference 26 discusses striation wave-lengths in the 100m - 1 km regime). Striation studies to resolve shorter and shorter wave-lengths, as well as the stopping of striation bifurcation and coupling to other ionospheric levels are ongoing.

B. Equatorial Spread F

Equatorial spread F (ESF) was discovered over four decades ago[33] as diffuse echoes on ionograms. Notwithstanding this fact, it is only recently that our understanding of this phenomena has increased dramatically (see references 1-4). Before we proceed let us examine the basic equatorial F region geometry. Figure 5 depicts the geometry under which ESF occurs. N(y) represents the background zero order electron density as a function of altitude (y). Gravity $\underline{g}$ points down, the ambient geomagnetic field $\underline{B}$ is horizontal and pointing north (z), and k represents a horizontal perturbation vector and points westward (x). The maximum in electron density defines the F peak. The bottomside of the profile steepens at night due to chemical recombination effects and upward ambient

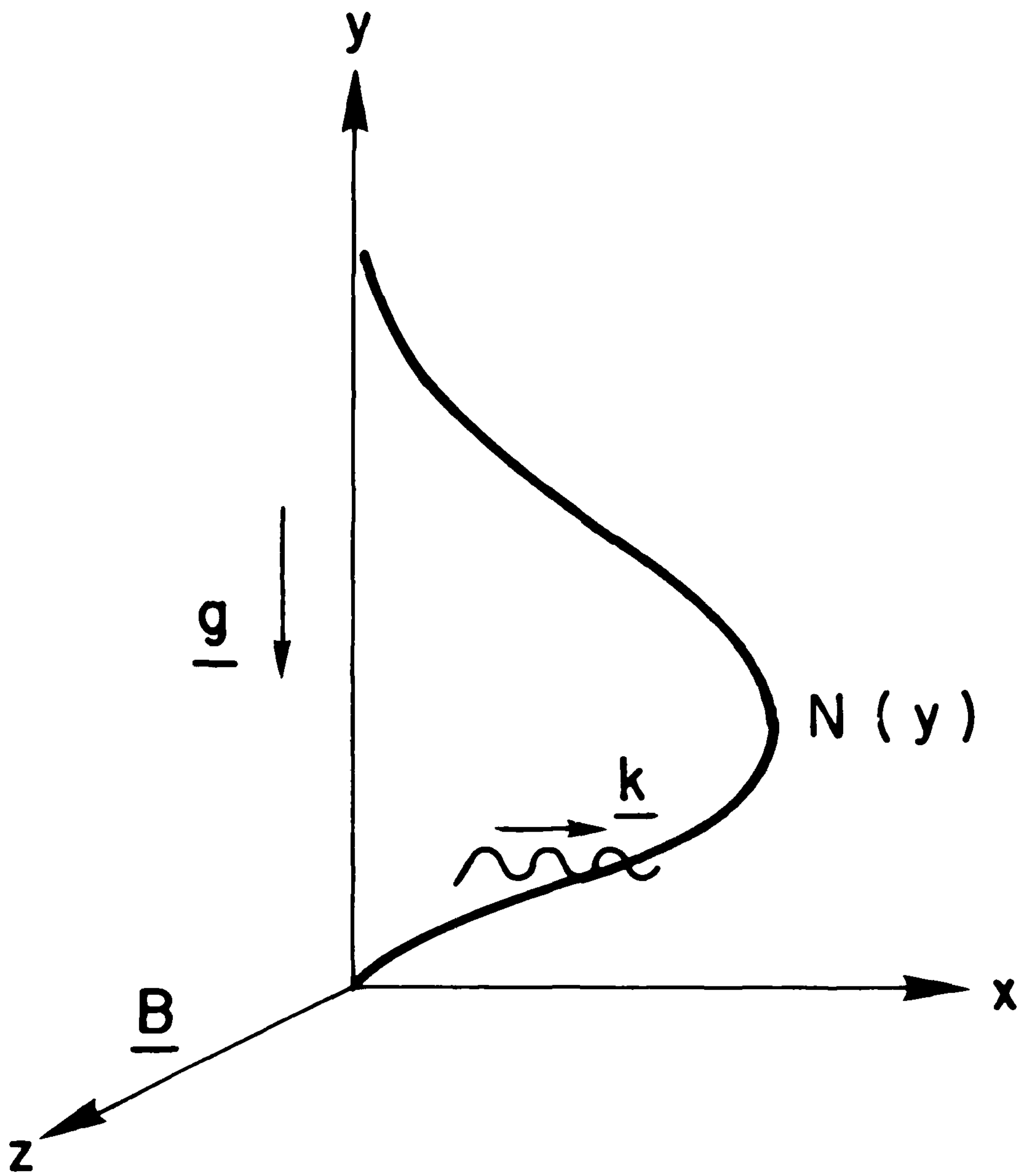

Fig. 5 — Basic equatorial spread F geometry

$\underline{E} \times \underline{B}$ electrodynamic forces. One might expect this equatorial ionospheric geometry to be unstable to a variety of plasma instabilities because in the plasma physics community Figure 5 represents the classical flute mode geometry. It is reminiscent of a heavy fluid (higher density region on the bottomside) being supported by a light fluid (low density region on the bottomside).

In the past few years much effort has been expended to describe and explain equatorial spread F phenomena both from an experimental and theoretical viewpoint[1-4]. It is now generally believed that the collisional Rayleigh-Taylor instability mechanism (or possibly the $\underline{E} \times \underline{B}$ gradient drift instability; in any case a fluid type gradient instability) initiates equatorial spread F in the bottomside evening equatorial F region ionosphere[1-4]. Several experimental results lend credence to this idea[34-37]. The generation of this instability on the bottomside leads to the formation of plasma density depletions (bubbles), which then rise to the topside. These bubbles were predicted by the nonlinear numerical simulation studies (in the collisional Rayleigh-Taylor regime, denoted CR-T) of Scannapieco and Ossakow[38] and have been observed experimentally.[34-37,39-41] The initial nonlinear numerical studies[38] showed how a plasma mode (CR-T), which is linearly unstable on the bottomside only, could, by nonlinear polarization $\underline{E} \times \underline{B}$ forces in the equatorial geometry, produce bubble induced irregularities on the topside, where the mode is linearly stable. These initial simulation studies represented a major break-through in the undertaking of ESF phenomena for they answered the following age old questions. (1) Why are plasma density fluctuations observed on both sides of the F peak when linear theory of the representative instabilities predict only bottomside growth (unstable)? (2) Why does the onset of topside ESF lag the onset of bottomside ESF? Other numerical simulation studies of large scale bubble phenomena have been performed[42-44] as well as intermediate wavelength studies[45-46] which examine a chunk of the bottomside ESF ionosphere to obtain power spectra for irregularity wavelengths in the 100 m-1 km regime. These studies help to answer the following additional questions. (3) How are the large plasma depletions (bubbles) produced? (4) What causes the westward tilts of the bubbles and the observed radar backscatter plumes? (5) What is the power spectrum for the plasma irregularities during FSF?

We will now apply (1)-(5) to the two dimensions perpendicular to $\underline{B}$ at the geomagnetic equator, making various approximations. If inertial terms are neglected (i.e., the left hand side of (2)), take $\nu_{in}/\Omega_i << 1$ (valid in the F region approximation), neglect R_α in (2), neglect $\underline{U}$, and use the quasi-neutral approximation, $n_e \approx n_i \approx n$, then (1)-(2) become for the two dimensions (x,y) perpendicular to $\underline{B}$

$$\frac{\partial n_\alpha}{\partial t} + \nabla\cdot(n_\alpha \underline{V}_\alpha) = -\nu_R(n_\alpha - n_{\alpha o}) \tag{14}$$

$$\underline{V}_e = \frac{c}{B}\underline{E} \times \hat{\underline{z}} \tag{15}$$

$$\underline{V}_i = \left(\frac{\underline{g}}{\Omega_i} + \frac{c}{B}\underline{E}\right) \times \hat{\underline{z}} + \frac{\nu_{in}}{\Omega_i}\left(\frac{\underline{g}}{\Omega_i} + \frac{c}{B}\underline{E}\right) \tag{16}$$

where we have neglected neutral wind effects, $\Omega_i = eB/m_i c$, $\underline{B} = B\hat{\underline{z}}$ and we have set $T_e = T_i = 0$ for simplicity (see reference 42). It should be noted that the term $\nu_R n_{\alpha o}$ on the right hand side of (14) represents an effective ionization source such that $n_{\alpha o}(t) = n_{\alpha o}(0)$, i.e., that the zero order distribution changes on a much longer time scale than any perturbations.[42,43] The $\underline{g} \times \hat{\underline{z}}$ motion in (15) has been neglected compared with the same ion motion because they are in the ratio m_e/m_i. Making the electrostatic approximation $\underline{E} = -\nabla\phi$ and setting $\phi = \phi_o + \tilde{\phi}$, where the subscript zero refers to equilibrium or zero order quantities and the tilde again refers to perturbed quantities, we obtain (with $n_e \approx n_i \approx n$)

$$\frac{\partial n}{\partial t} - \frac{c}{B}(\nabla\tilde{\phi} \times \hat{\underline{z}})\cdot\nabla n = -\nu_R(n - n_o) \tag{17}$$

$$\nabla\cdot(\nu_{in} n \nabla\tilde{\phi}) = \frac{B}{c}(\underline{g} \times \hat{\underline{z}})\cdot\nabla n \tag{18}$$

In arriving at (18) we have put (15) and (16) into (4) and (5) and obtained $\nabla\phi_o = m_i \underline{g}/e$. Equation (9) can be viewed as the electron continuity equation in the $-\nabla\phi_o \times \underline{B}$ drift frame (i.e., $-\underline{g} \times \underline{\hat{z}}/\Omega_i$ frame). Equation (18) results from (4). Equations (17) and (18) are to be compared with (6) and (7). In their simplest forms (setting $\nu_R = D = 0$), the equations are quite similar. In (18) if we think of ν_{in} as a constant then (18) is identical with (7) if we interpret $(B/c\,\nu_{in})\,\underline{g} \times \underline{\hat{z}}$ as an effective electric field. To obtain a linear growth rate from (17) and (18) we set $n = n_o(y) + \hat{n}$ and put $\hat{n},\hat{\phi} \propto \exp i(\underline{k}\cdot\underline{x} - \omega t)$, where $k^2 = k_x^2 + k_y^2$ and $\omega \equiv \omega_r + i\gamma$. The growth rate γ then is, for $kL \gg 1$,

$$\gamma = \frac{g}{\nu_{in} L}\left(\frac{k_x}{k}\right)^2 - \nu_R \tag{19}$$

where $L^{-1} = \partial \ln n_o/\partial y$. For horizontal waves, i.e., $k = k_x$ this reduces to

$$\gamma = \frac{g}{\nu_{in} L} - \nu_R \tag{20}$$

Both (19) and (20) show that linear growth is possible only on the bottomside of the equatorial ionosphere depicted in fig. 5.

<u>Two-Dimensional Global Numerical Simulations.</u> In this section we will outline some two dimensional ($\perp \underline{B}$ and at the geomagnetic equator) numerical simulation results of the collisional Rayligh-Taylor mechanism[43]. The simulation plane encompasses an altitude extent of over 200 km (see fig. 6), from the bottomside to the topside of the ESF region. Ionospheric profiles of $n_o(y)$, $\nu_{in}(y)$, and $\nu_R(y)$ are used in the simulations. A simulation mesh of 140 (altitude, y) by 40 (east-west, x) was employed with $\Delta x = 5$ km (large case, L). In reference 43 studies were also performed with $\Delta x = 200$ m (small case, S). The boundary conditions were periodic in x and y transmittive for n ($\partial n/\partial y = 0$) and Neumann ($\partial\hat{\phi}/\partial y = 0$) for the induced potential $\hat{\phi}$. In these particular simulations n_o was set to zero in (17) so that n_o obeyed $\partial n_o/\partial t = -\nu_R n_o$ and (18) was

retained in tact. Two different types of initial perturbations and different wavelengths corresponding to the large case and small case were used (four cases in all). However, here we will only present case 1L, which is defined with $\Delta x = 5$ km and a perturbation of the form (see ref. 43 for more details).

$$\frac{n(x,y,0)}{n_o(y,0)} = 1 - e^{-3}\cos\left(\frac{\pi x}{8\Delta x}\right), \quad 0<|x|<8\Delta x$$

$$\frac{n(x,y,0)}{n_o(y,0)} = 1 - e^{-3}\,\frac{1}{2}\left[\cos\left(\frac{\pi x}{8\Delta x}\right) - 1\right],$$

$$8\Delta x < |x| < 16\Delta x$$

$$\frac{n(x,y,0)}{n_o(y,0)} = 1, \quad |x|>16\Delta x \tag{21}$$

In contrast to this more localized type of perturbation which has been used before[42] the pure sinusoidal one, also used in ref. 43, will not be shown here. [Note: The perturbation for the pure sinusoid is given as $n(x,y,0)/n_o(y,0) = 1 - e^{-3}\cos(\pi x/20\Delta x)$. This different type of non-localized perturbation was chosen to contrast with (21). The results produced for bubble rise, etc. are similar in nature with some slight differences over the results obtained using (21). For the sake of brevity the reader is referred to reference 43 for more details.]

Figure 6 shows isodensity contours of calculation 1L at times 300, 700, 1000 and 1200 sec after initialization. While the initial perturbation (21) is put over the entire altitude (y) extent of the mesh, we see from 300 to 700 sec that the perturbation grows on the bottomside, but damps on the topside as it should according to (20). The build-up of the bubble is evident in the 1000 and 1200 sec plots. At 1200 sec figure 6 shows a single plume of depleted ionization with no secondary central bubble or side bubble. In figure 7 a plot of $n(x,y)/n_o(y)$ for case 1L at 1200 sec is exhibited. The level of depletion is greater than 99.9% for

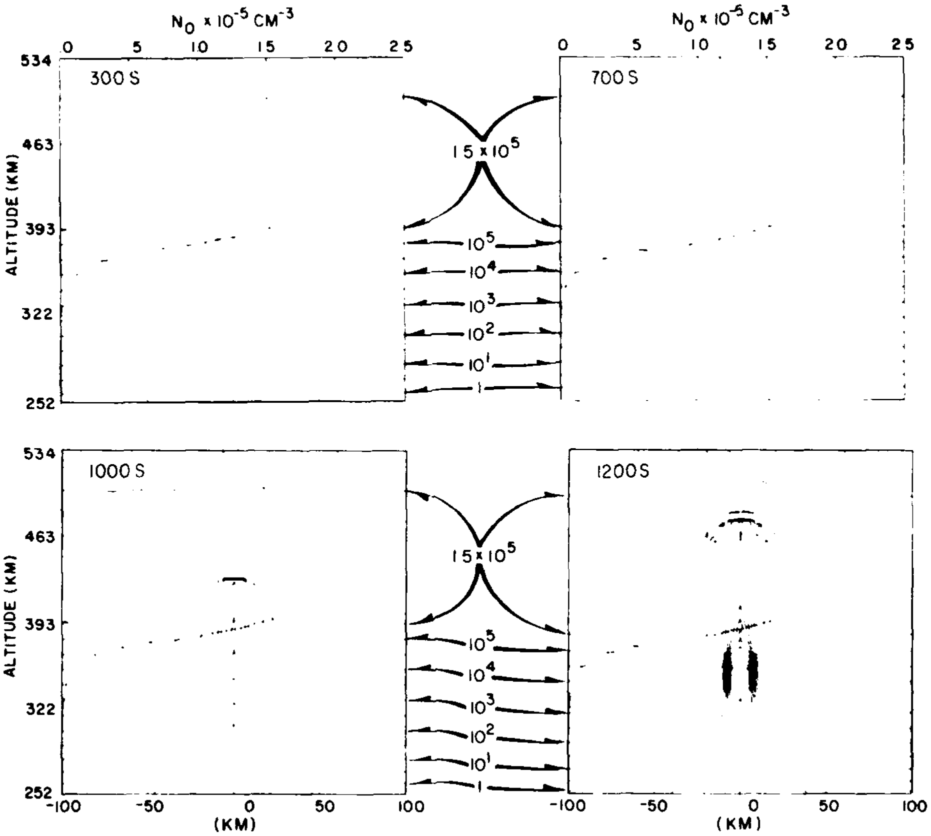

Fig. 6 — Sequence of four plots showing isoelectron density contours of calculation 1L at 300, 700, 1000, and 1200 sec. Superimposed on each plot is a dashed line showing $n_0(y,t)$ and labeled at the top. Electron densities are given in units of cm^{-3}. The observer is looking southward so that B is out of the figure (after ref. 43).

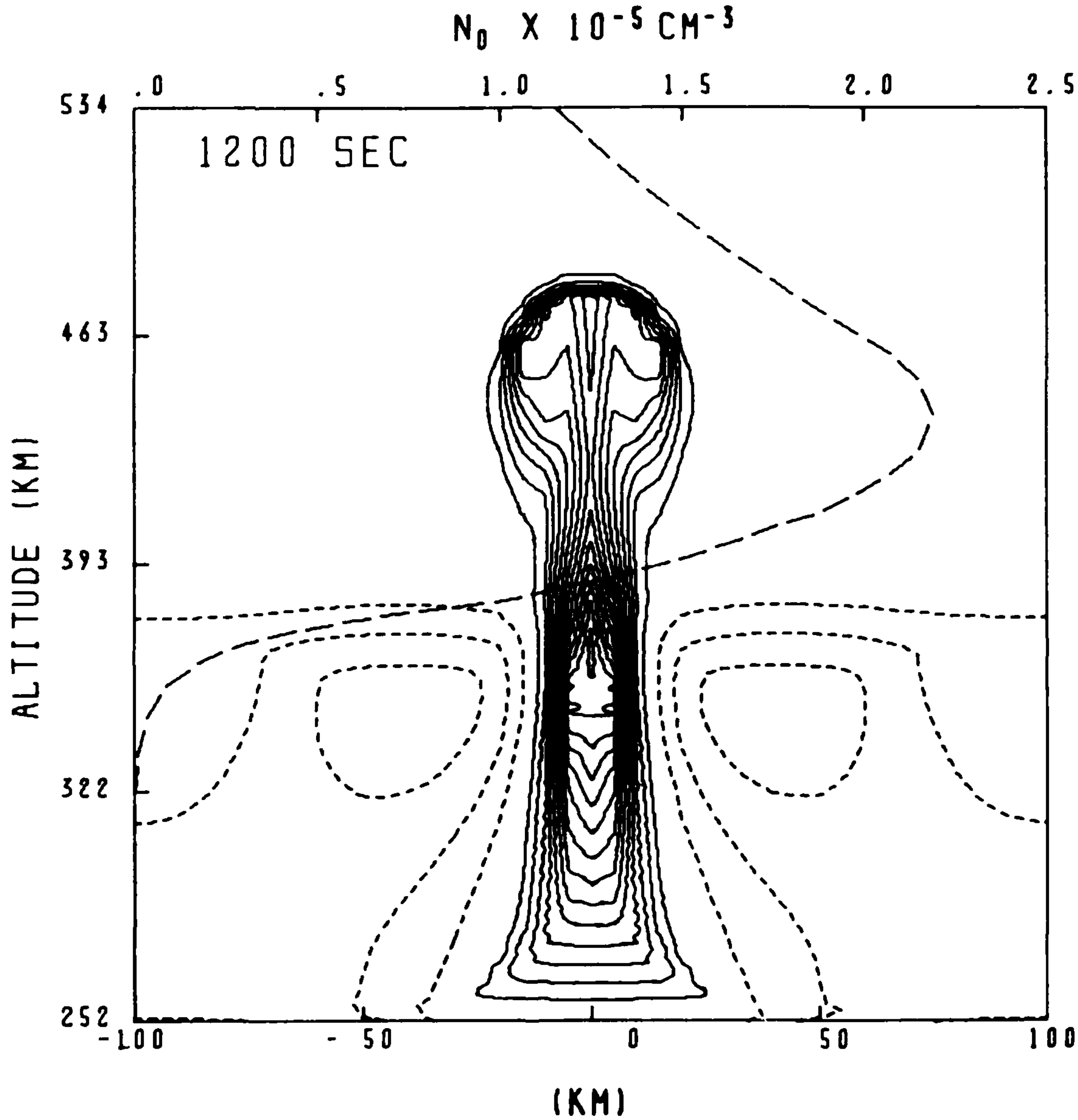

Fig. 7 — Contours of constant $n(x,y,t)/n_0(y,t)$ for 1L at 1200 sec. Depletions $(n/n_0<1)$ are shown in solid lines while enhancements $(n/n_0>)$ are shown as short dashed lines. The first (outermost) depletion contour is for n/n_0 = 0.5, while each succeeding contour is for a value of n/n_0 a factor of 0.5 times the previous one. The first enhancement contour is for n/n_0 = 2.0, while each succeeding contour is for a value of n/n_0 a factor of 2.0 times the previous one. The superimposed long dashed line depicts $n_0(y,t)$ (after ref. 43).

the entire 10 by 70 km oval hole located inside the tenth solid contour and represents at least a three orders of magnitude decrease (bite-out) in plasma density. The bubble rise velocity, computed from the last two frames of fig. 6, is 230 m/s. These large bite-outs and large rise velocities are in agreement with the observations of McClure et al.[35] The reason that the bubble is so depleted in the 1L case can be seen with the aid of fig. 8. This shows the induced electrostatic potential $\tilde{\phi}$ at 700 sec. We notice that the fringe field surrounding the bubble extends to low altitudes (lower than say the 1S case in ref. 43). Since the contours of constant potential are in fact flow streamlines, much plasma is being drawn up from low altitudes (see fig. 6). The effect is similar to the fringe field of a parallel plate capacitor. In the case depicted in fig. 8 the role of plate separation is played by the horizontal scale size of the bubble (see ref. 43 for more details). We also note that the induced potential is such as to make the induced electric field point from right (west) to left (east) so that the induced $\underline{E} \times \underline{B}$ motion is upward.

Summary. In this section we have shown how plasma fluid equations are used to study, by numerical simulation methods, the nonlinear evolution of equatorial spread F phenomena, driven by the collisional Rayleigh-Taylor instability mechanism. To keep things simple we have exhibited the pure collisional R-T regime, i.e., horizontal zero order neutral winds and/or electric fields have not been included in the study. The results gleaned from these numerical simulations of large horizontal wavelength initial perturbations in the collisional R-T regime are as follows. The large scale length initial perturbations evolve nonlinearly into large horizontal scale length ESF bubbles. These bubbles rise up from the bottomside to the topside and evolve approximately on the same time scale as do the smaller horizontal scale length counterparts[42,43]. The plasma comprising these large bubbles has its origin at very low altitudes (much lower than that of the smaller horizontal scale length bubbles) and this results in plasma density depletions in the large bubbles very close to 100%, i.e., several orders of magnitude depletions. These results are consistent with experimental results[1-4,34-37,39-41]. Studies to investigate shorter wavelength ESF phenomena, via analytic and numerical simulation methods, have been ongoing[1-4,45-46], including the decay[47] of these ESF irregularities. Large scale global numerical simulations[44] have been

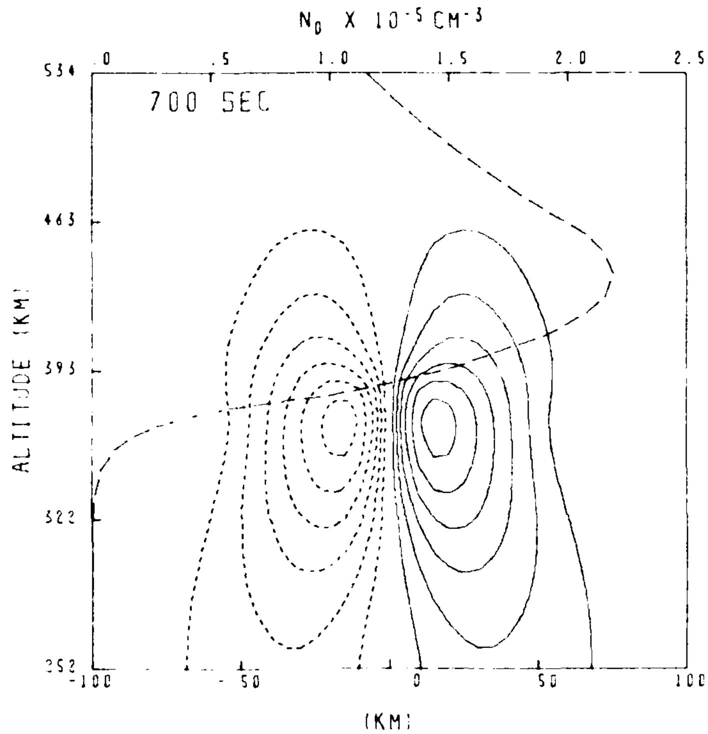

Fig. 8 — Contours of constant induced electrostatic potential at 700 sec for calculation 1L. Small dashed lines are for negative potentials and solid lines are for positive potentials. The potential drop, across adjacent contours is a constant except that the zero potential is not plotted. The contours are chosen to space the twelve contours (plus the zero contour) uniformly from maximum to minimum potential. The large dashed line depicts $n_0(y)$ at 700 sec (after ref. 43).

started which incorporate the effects of background Pedersen conductivity (another level, similar to plasma cloud striation studies) and an F region neutral wind, at the equator, blowing to the east. Results from this study[44] show that the first effect can slow down ESF and the attendant bubble rise phenomena and the neutral wind effect in combination with the first effect can result in a westward tilt of the bubbles[35-37] and attendant radar backscatter plumes[36,37]. Also, the studies[44] show that solution of the zero order or equilibrium equations result in a plasma velocity shear as a function of altitude. This shear is in agreement with recent radar backscatter studies[48-49] of ESF phenomena.

Even though work is still continuing on ESF phenomena, a basic physical picture of ESF that emerges through theoretical, numerical simulation and experimental studies is as follows. After sunset the F-region begins to recombine and there is effectively no F-region conductivity to short out any irregularities in the F-region. Due to recombination and possible electrodynamic effects (upward motion of the F-region plasma due to $\underline{E} \times \underline{B}$) the bottomside F-region background electron density gradient begins to steepen. The steepening due to plasma $\underline{E} \times \underline{B}$ uplift caused by an eastward electric field is much like barium cloud steepening in equatorial geometry (note a downward motion of the neutral atmosphere will have the same effect). When the altitude of the F-region is high enough and/or the bottomside background electron density gradient steep enough to overcome recombination effects, plasma density fluctuations will begin to grow on the bottomside via the collisional Rayleigh-Taylor instability mechanism (or possibly initiated by the $\underline{E} \times \underline{B}$ gradient drift instability). These irregularities will in turn form plasma density depletions (bubbles) on the bottomside which will then nonlinearly rise by polarization $\underline{E} \times \underline{B}$ motion through the F peak and cause topside spread F. (The higher the F peak and/or the sharper the bottomside gradient, and the higher the percentage depletion the faster the rise rate of the bubble and the faster the evolution of ESF). These steepening bubbles (on their topside) can then bifurcate and form smaller scale structure by a cascade or two-step mechanism. An eastward neutral wind can cause the bubbles to move westward with respect to the bulk plasma motion. The long wavelength irregularities have a power law PSD $\propto$ k^{-2} ? It is presently believed that the small scale ($\lesssim$ 3 m) radar backscatter observed irregularities (kinetic

type instabilities) are created by the primary long wavelength fluid type instabilities (collisional Rayleigh-Taylor, etc.). The turn on and turn off of these very small scale irregularities and their connection to the longer wavelength irregularities is not well understood at present and requires further investigation (see ref. 3 for more details).

C. High Latitude Diffuse Auroral Irregularities

DNA Wideband satellite observations have exhibited a regularly occurring scintillation enhancement in the auroral zone data, in the region of diffuse auroral particle precipitation.[50-53] The scintillation data have indicated that the enhancement is due to sheet-like, L shell aligned F region ionospheric irregularities[50,51]. In the initial experimental results[50,51], the irregularities occurred where there was a strong northward total electron content (TEC) gradient. Associated with the northward TEC gradient is a northward gradient in local F region plasma density[53,54] as measured by the Chatanika radar. In addition, measurements show a d.c. electric field pointing westward or northwest and a very shallow altitude plasma density gradient,[54] i.e., the northward TEC gradient dominates. Later experimental results[54] showed large scale equatorward convecting enhancements, limited in latitudinal extent with steep poleward and equatorward edges (two-sided, much like a large barium cloud).

At first sight, with the dominant plasma density gradient pointing northward, the ambient magnetic field, $\underline{B}$, pointing down and the d.c. electric field horizontal (see fig. 9), this would appear to be a prime geometry for the usual F region $\underline{E} \times \underline{B}$ gradient instability (see subsection A and fig. 1). However, with the d.c. electric field pointing westward or northwest, the configuration is stable (the electric field would have to point eastward for instability). The saving feature, however, is the diffuse auroral precipitation resulting in a current along $\underline{B}$, which acts to destabilize the above geometrical configuration[55]. The conditions of having a current along $\underline{B}$, a density gradient, ∇n_o perpendicular to $\underline{B}$ can result in instability and these types of instabilities are generically called current convective instabilities[56] (CCI). The instability has $k_\parallel << k_\perp$ (see next section) and so the irregularities generated will be magnetic field aligned. This current convective instability can directly

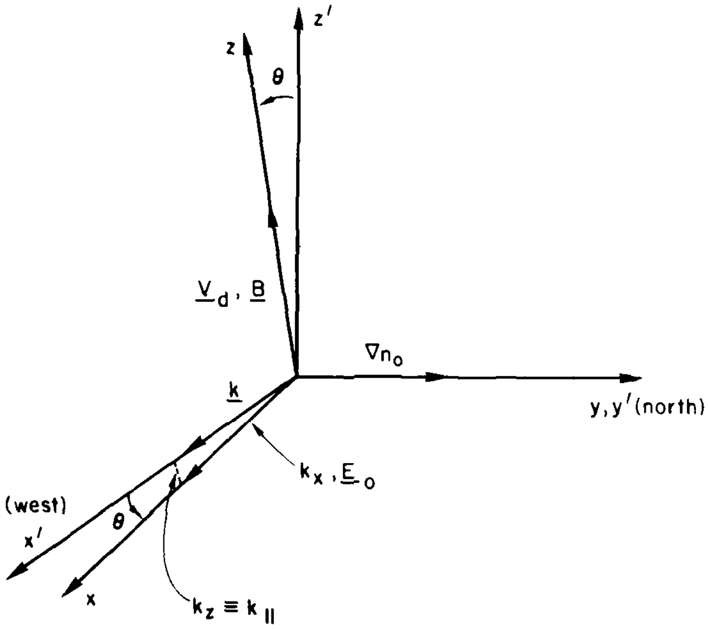

Fig. 9 — Basic current convective instability geometry and coordinate system used in the simulations. The x'y' plane is the simulation plane. The x',x,z',z axes are coplanar (after ref. 60).

result in long wavelength scintillation causing F region ionospheric irregularities in the diffuse auroral region. A nonlinear mode coupling theory has been applied[57] to the CCI to look at saturation of the instability. In addition, the linear theory[55] of the CCI has been extended to include magnetic shear effects[58], highly collisional (non-magnetized) ions (e.g., the E region)[59], electromagnetic effects[59], and ion inertial effects[59], which extends the instability to higher F region altitudes. Numerical simulations of diffuse auroral F region irregularities have been performed for one-sided density gradients[60] (where the CCI is dominant), as well as two-sided density gradients[61] (where the $\underline{E} \times \underline{B}$ gradient drift instability is dominant on the poleward gradient side, with the CCI adding to the instability). In this paper, in order to emphasize the nature of the CCI instability, results from the former numerical simulation[60] will be presented.

Now we present a theoretical model[55] for a long wavelength fluid type plasma instability which may account for the scintillation causing diffuse auroral F region ionosphere irregularities. For our model we take the electron density gradient to be pointing northward (y), the ambient electric field $\underline{E}_o$ is in the westward direction (x) and the magnetic field points downward (z). In our simple model we have equated the TEC gradient with a gradient in plasma density. We assume that the horizontal (northward) electron density gradient is much sharper than the altitude density gradient, which we neglect. Our basic equations, from (1)-(5), are

$$\frac{\partial n_\alpha}{\partial t} + \nabla\cdot(n_\alpha \underline{V}_\alpha) = 0 \tag{22}$$

$$\underline{V}_i = \frac{c}{B}\,\underline{E} \times \hat{z} - \frac{c}{B}\frac{\nu_i}{\Omega_i}\,\underline{E}_\perp + \frac{c}{B}\frac{\Omega_i}{\nu_i}\,\underline{E}_\parallel + \underline{V}_{io\parallel} \tag{23}$$

$$\underline{V}_e = \frac{c}{B}\,\underline{E} \times \hat{z} - \frac{c}{B}\frac{\Omega_e}{\nu_e}\,\underline{E}_\parallel + \underline{V}_{eo\parallel} \tag{24}$$

and (5), where we have neglected inertial effects (left hand side of (22)), $\underline{\hat{z}} = \underline{B}/|B|$, $\Omega_\alpha = |e_\alpha|B/m_\alpha c$, $V_{\alpha o\parallel}$ represents the diffuse auroral particle

precipitation induced velocity along $\underline{B}$ ($\parallel$ and $\perp$ denote parallel and perpendicular to $\underline{B}$) which results in a zero order current and the other symbols have their usual meaning. In addition, we have neglected temperature and neutral wind effects and included electron collisions to first order for completeness. Equations (23) and (24) are valid for F region ionospheric altitudes such that $\nu_\alpha/\Omega_\alpha << 1$. In (23) ν_i is taken to mean ion-neutral collisions, while in (24) ν_e is really electron-ion collisions. In (24) the electron Pedersen drift has been neglected, compared with the ion Pedersen drift in (23). Making the usual quasi-neutrality assumption, $n_e \approx n_i \approx n$, the final equations from (22), (23), (24) and (5) are

$$\frac{\partial n}{\partial t} + \frac{c}{B} (\hat{\underline{z}} \times \nabla\tilde{\phi})\cdot\nabla n - \frac{c}{B} \quad \nabla\cdot(n$$

$$(\frac{\nu_i}{\Omega_i} \quad \nabla_\perp\tilde{\phi} + \hat{\underline{z}} \quad \frac{\Omega_i}{\nu_i} \quad \frac{\partial\tilde{\phi}}{\partial z})) = 0 \tag{25}$$

$$\nabla\cdot(n[\nabla_\perp\tilde{\phi} + \hat{\underline{z}} \left((\frac{\Omega_i\Omega_e}{\nu_i\nu_e})^2 + (\frac{\Omega_i}{\nu_i})^2 \right) \frac{\partial\tilde{\phi}}{\partial z}])$$

$$= (\underline{E}_o - \frac{\Omega_i}{\nu_i} \frac{B}{c} \underline{V}_d)\cdot\nabla n \tag{26}$$

where $\nabla\tilde{\phi} = \underline{E} - \underline{E}_o$ with $\underline{E}(x,y,z,t)$ the total electric field and $V_d = V_{io\parallel} - V_{eo\parallel}$. Equations (25) and (26) are simply a restatement of the ion-continuity equation written in a reference frame with velocity $\underline{V}_o = -E_o/B(\hat{\underline{y}} - \nu_i/\Omega_i \; \hat{\underline{x}})$ and quasi-neutrality $\nabla\cdot \underline{J} = 0$, respectively. In (25) and (26) $\nabla \equiv (\partial/\partial x, \partial/\partial y, \partial/\partial z)$ and $\nabla_\perp \equiv (\partial/\partial x, \partial/\partial y)$. We note the similarity between (25), (26) and (6), (7), and (17), (18). If we set $V_d = 0$ and $\partial/\partial z = 0$ in (25) and (26) then we recover the simplest form of the $\underline{E} \times \underline{B}$ gradient drift instability, equations (simplest form of (6) and (7)).

Equations (25) and (26) are then linearized such that $n = n_o(y) + \hat{n}$, $\underline{E} = E_o\hat{\underline{x}} - \nabla\hat{\phi}$, $\underline{V}_\alpha = \underline{V}_{\alpha o} + \hat{\underline{V}}_\alpha$ with the perturbed quantities $\hat{n}$, $\hat{\underline{V}} \propto \exp i[k_x x + k_\parallel z - \omega t]$, where $\omega \equiv \omega_r + i\gamma$. We then obtain

$$
\gamma = \frac{-\frac{1}{n_o}\frac{\partial n_o}{\partial y}\left[\frac{c}{B} E_o \frac{\nu_i}{\Omega_i} + V_d \frac{k_\parallel}{k_x}\right]}{\left[\frac{\Omega_i}{\nu_i} + \frac{\Omega_e}{\nu_e}\right] \frac{k_\parallel{}^2}{k_x{}^2} + \frac{\nu_i}{\Omega_i}} \tag{27}
$$

where $V_d = V_{io\parallel} - V_{eo\parallel}$. We see that in (27) γ is independent of $|k|$ and only depends on the angle that k makes with $\underline{B}$. In the denominator of (27), the first term (in brackets) multiplying $(k_\parallel/k_x)^2$ comes from the parallel motion of the ions and electrons; whereas, the remainder of the denominator comes from the ion Pedersen motion. It should be noted that the instability is essentially unaffected by the current direction. Thus, downward currents work just as well as upward currents. In (27) if we set $k_\parallel = 0$ we obtain $\gamma = -(n_o{}^{-1}\partial n_o/\partial y)(cE_o/B)$ which is the usual result for the $\underline{E} \times \underline{B}$ gradient drift instability. For our geometry this shows γ is negative which implies stability. For instability in (27) $\gamma > 0$ which implies

$$
\frac{c}{B_o} E_o \frac{\nu_i}{\Omega_i} + V_d \frac{k_\parallel}{k_x} < 0 \tag{28}
$$

This says that for instability, with the westward $\underline{E}_o$, we must have $V_d k_\parallel/k_x < 0$ and $|V_d k_\parallel| > (k_x cE /B)(\nu_i/\Omega_i)$. We can maximize this growth with respect to $\theta \equiv k_\parallel/k_x$. From (27) the growth rate maximizes, in general for

$$
\theta = -(cE_o/B\ V_d)(\nu_i/\Omega_i) \pm
$$

$$
\{(cE_o/B\ V_d)^2(\nu_i/\Omega_i)^2 +
$$

$$
(\nu_i/\Omega_i)[(\Omega_i/\nu_i) + (\Omega_e/\nu_e)]^{-1}\}^{1/2} \tag{29}
$$

For altitudes ~ 350–400 km corresponding to the observation altitudes[51] $\nu_i/\Omega_i \sim 10^{-4}$, $\nu_e\Omega_e \sim 10^{-4}$, and $E_o \sim 10$ mV/m with $V_d \sim -500$ m/sec we find $\theta = 9.4 \times 10^{-5}$. For this case (27) gives a growth rate $\gamma_{max} \simeq 2.7 \times 10^{-3}\text{sec}^{-1}$ for $L \equiv n_o(\partial n_o/\partial y)^{-1} \sim 50$ km. Including pressure effects in the problem introduces diffusive damping in (27). A typical cross-field diffusion coefficient, $D_\perp$, is ~ 0.2 m^2/sec and a parallel diffusion coefficient, $D_\parallel$, is ~ 10^8 m^2/sec. In the present study, these effects become important for perpendicular wavelengths, $\lambda_\perp$, $\lesssim$ 100 m and parallel wavelengths, $\lambda_\parallel$, $\lesssim$ 1000 km. However, typical scintillation causing perpendicular wavelengths are ~ 1 km and since $k_\parallel/k_\perp \sim 10^{-4}$ we are considering highly field aligned irregularities. Larger parallel currents, due to precipitation, will of course produce larger growth rates. However, too large a current, $V_d \gtrsim 1$ km/sec, would excite the collisional electrostatic ion cyclotron instability[62]. It may be noted that the linear theory of the current convective instability proposed here favors a wavevector perpendicular to the TEC gradient (as well as $\underline{B}$). However, in the nonlinear regime, mode coupling theory suggests[57] that the dominant wavevectors will lie parallel to the TEC gradient (and local F region plasma density gradient) thus accounting for the L-shell aligned nature of these irregularities[51,53]. Basically in this theory, the current convective instability saturates (stabilizes) nonlinearly by generating linearly damped harmonics (i.e., those along the northward plasma density gradient). These harmonics dominate over those between the northward and east-west directions. In addition, these northward modes produce a power spectrum for the irregularities $\propto k^{-2}$.

Diffuse Auroral Numerical Simulations. In the following simulations we take advantage of the fact that the fastest growing, most dangerous modes from linear theory are almost field-aligned ($k_\parallel/k_\perp \ll 1$). These modes are of most interest to us and, as a result, we solve equations (25) and (26) in a plane containing these modes which is nearly perpendicular to the magnetic field while fixing the value of $k_\parallel/k_\perp$ (see ref. 60). A similar approach has been adopted in numerical studies of drift-wave[63] and trapped-particle[64] instabilities in laboratory plasmas. The simulation plane which is essentially horizontal at an altitude of 350 km with a

north-south extent of 410 km and an east-west extent of 160 km is identical to the $x'y'$ plane as shown in Figure 9. The system of equations (25) and (26) was transformed[60,61] to the $x'y'z'$ coordinate system by a simple rotation about the y-axis by the angle $\theta = k_{\parallel}/k_x \ll 1$. By solving the equations (25) and (26) in the $x'y'z'$ system a finite but small $k_{\parallel}$ is effectively introduced into the model. After neglecting the z'- dependence of all quantities, equations (25) and (26) were then cast into dimensionless form and initialized with the profile of the following type $n_o(y')/N_o = (1-A(1-\tanh(y'-y_o)/L))\,(1 + \varepsilon(x',y'))$ where N_o, y_o, and L are constant with A = 5/11. This gives a total density maximum to minimum ratio of approximately 10. The function $\varepsilon(x',y')$ has a root-mean-square value of 3% and is generated from a randomly phased Gaussian power spectrum. The computational mesh consisted of 258 grid points in the y'- direction (north-south) with 102 points in the x'- direction (east-west) so that $\Delta y = \Delta x = 1.6$ km. Periodic boundary conditions were imposed in the x'- direction with Neumann $(\partial/\partial y' = 0)$boundary conditions in the y'- direction. We now drop the prime notation for clarity.

Figure 10 shows contour plots of $n(x,y)/N_o$ at t = 0, 900, 1400, 1900 sec. The following set of parameters were used: L = 50 km, y_o = 200 km, E_o = 10 mV/m, $\nu_i/\Omega_i = 10^{-4}$, $\nu_e/\Omega_e = 10^{-4}$. The value of $\theta = 9.4 \times 10^{-5}$ is held fixed and is chosen so as to maximize the linear growth rate (27). Figure 10 at t = 0 shows the initial configuration which includes the small random perturbation. Figure 10 at t = 900 sec($\gamma_k t \simeq 5$) illustrates the linear stages of the simulation and shows unstable growth in the region where $\partial n_o/\partial y > 0$ as predicted by linear theory. Figure 10 at t = 1400 sec exemplifies the early nonlinear regime where lower density plasma (depletions) are moving in the positive y-direction (poleward) while higher density plasma (enhancements) are convecting in the negative y-direction (equatorward). The approximate velocities of the depletions and enhancements are 270 m/sec and 30 m/sec, respectively. Finally, well-developed steepened enhancements and depletions (of over 90%) are seen in Fig. 10 at t = 1900 sec. This late-time configuration is reminiscent of the motion of depletions (bubbles) moving vertically in the equatorial F region[38] and enhancements (striations) in ionospheric F region plasma clouds[22]. The length scales in Figure 10 are distorted with the depletions and enhancements longer and narrrower than is depicted. Similar linear and

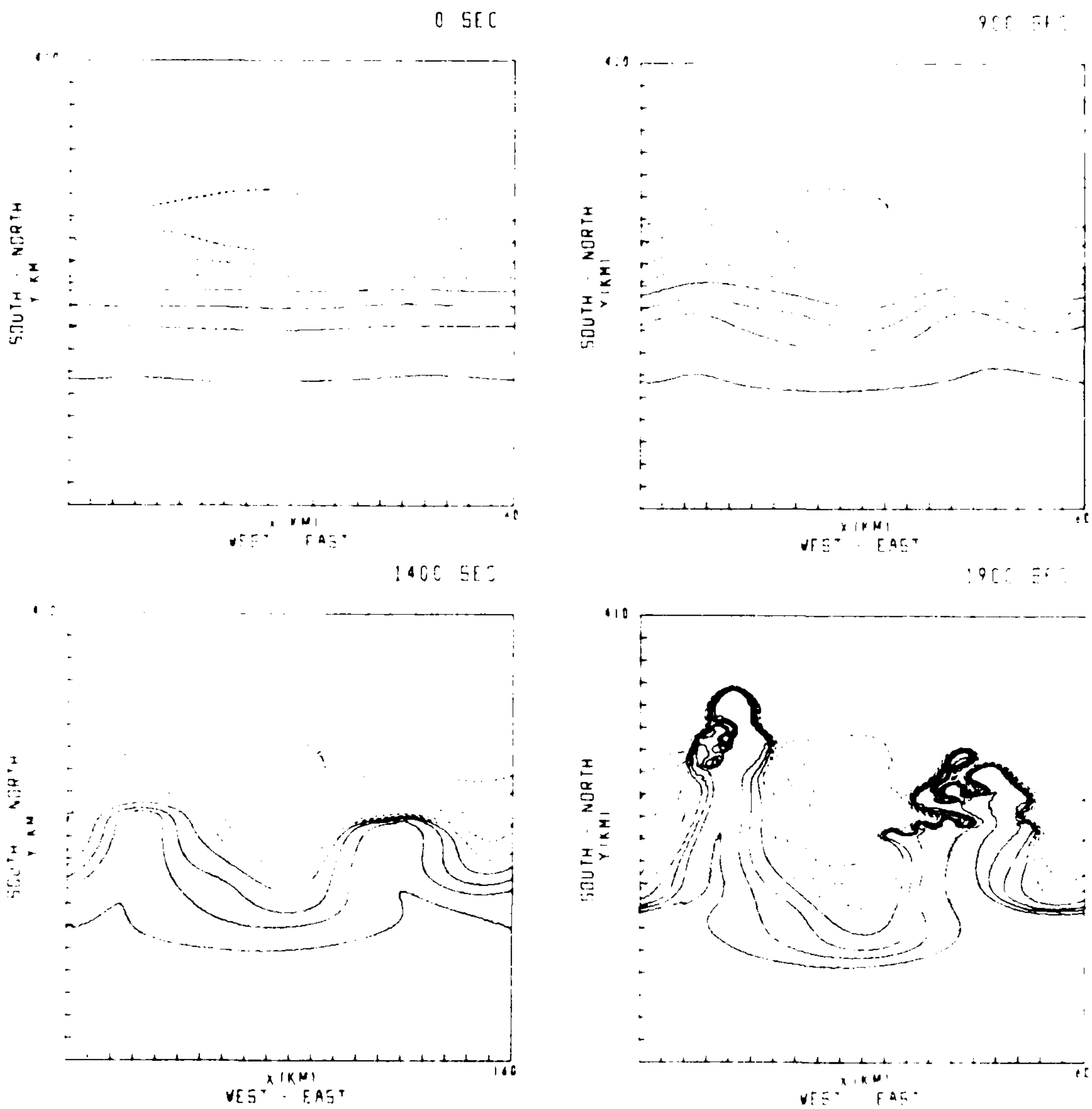

Fig. 10 — Real space isodensity contour plots of $n(x,y)/N_0$ for L = 50 km at t = 0, 900, 1400 and 1900 sec. Eight contours are plotted in equal increments from 1 to 10 with the lower (higher) density contours denoted by solid (dashed) lines. The magnetic field B is directed into the figure with the observer looking down the magnetic field lines toward the earth (after ref. 60).

nonlinear development is observed when $L = 10$ km, but on a faster time scale. Figures 11a-11b give sample one-dimensional spatial power spectra at $t = 1900$ sec both in the x-direction (east-west) and in the y-direction (north-south). These spectra are obtained by first Fourier analyzing $\delta n(x,y)/N_o$ and integrating over the direction in $\underline{k}$-space corresponding to the north-south and east-west directions, respectively (see (11) and (12)). For both cases, these power spectra are well-fitted with an inverse power law. Similar power law dependences were seen when $L = 10$ km.

The following physical picture of the evolution of current convective instability in the diffuse aurora is supported by these simulations. In the evening a westward electric field $\underline{E}_o$ begins to form which convects plasma in the auroral region equatorward. In regions where the northward gradient in total electron content becomes well-defined nearly field-aligned fluctuations ($k_\parallel/k_\perp \ll 1$) will grow unstable in regions where the field-aligned current velocities V_d, caused by precipitating particles, are such that $V_d(k_\parallel/k_\perp) > 0$ and $|V_d k_\parallel| > (k_\perp c E_o/B)\ (\nu_i/\Omega_i)$. In the plane almost perpendicular to the magnetic field by an angle $\theta = k_\parallel/k_\perp$ plasma depletions and enhancements will move northward and southward, respectively, while steepening in the process.

Summary. We have investigated analytically and numerically a simple plasma fluid model to account for the diffuse auroral scintillation causing F region ionospheric irregularities observed by the DNA Wideband satellite[57]. By taking account of the diffuse auroral particle precipitation (current) the stable $\underline{E} \times \underline{B}$ diffuse auroral geometry (corresponding to the observations) becomes destabilized by this parallel current. For a westward ambient d.c. electric field, $\underline{E}_o$, and a northward dominant electron density gradient, the relative drift velocity between ions and electrons parallel to B, V_d, must satisfy the condition $-\underline{k}\cdot\underline{V}_d > \underline{k}\cdot(c\underline{E}_o/B)\ (\nu_i/\Omega_i)$ for instability. The maximum growth rate for the instability is $\gamma \approx n_o^{-1}(\partial n_o/\partial y)V_d[1 + \Omega_e\nu_i/\Omega_i\nu_e]^{-1/2}/2$. The instability is mainly field aligned ($k_\parallel \ll k_\perp$). The instability is fluid-like in nature and so can directly account for the long wavelength diffuse auroral scintillation causing F region irregularities. In addition, nonlinear numerical simulations of this instability, as presented above, indicate equatorward movement (convection) of plasma enhancements and

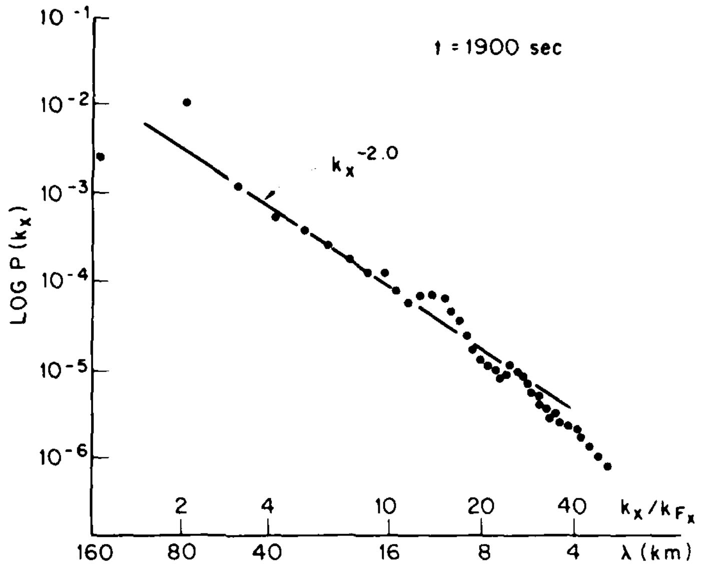

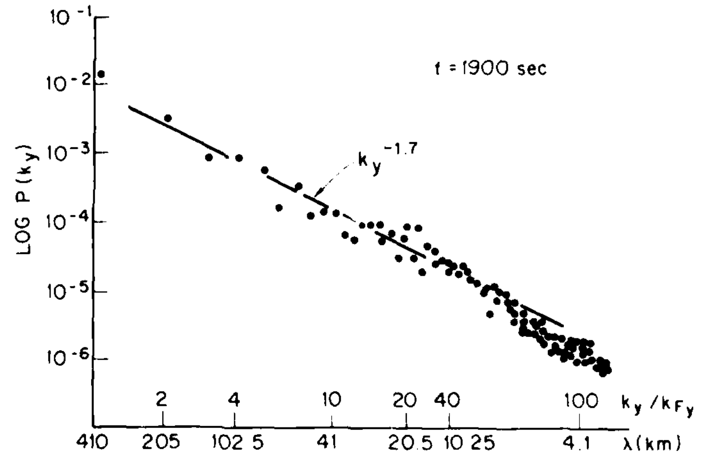

Fig. 11 — Log-log plots of one dimensional (a) x power spectrum $P(k_x)$ and (b) y power spectrum $P(k_y)$ for L = 50 km at 1900 sec. $P(k_x)$ and $P(k_y)$ are obtained by averaging $|\delta n(k_x,k_y)/N_0|^2$ over k_y and k_x respectively, where $\delta n(x,y) \equiv n(x,y)-N_0$. In (a) $k_{Fx} = 2\pi/160\ km^{-1}$ while in (b) $k_{Fy} = 2\pi/410\ km^{-1}$. The dots represent the numerical simulation results while the solid line is obtained from a least squares fit (after ref. 60).

northward (poleward) movement of plasma depletions (holes). Furthermore, one-dimensional spatial power spectra of the irregularities in both the north-south and east-west directions are well described by verse power laws $\propto k^{-2}$, for $\gamma \gtrsim 4$ km (the present wavelength range over which the simulations have been performed).

Analytic mode coupling theory has shown[57] that the instability can stabilize nonlinearly by generating linearly damped harmonics. With a northward plasma density gradient, the dominant nonlinear harmonic is in the northward direction; whereas, by linear theory the dominant mode would be in the east-west direction. The power spectral density (PSD) of the dominant nonlinear mode is $\propto k^{-2}$. The nonlinear evolution of two-sided (poleward and equatorward plasma density gradients) plasma enhancements in the presence of field aligned currents and ambient auroral electric fields of arbitrary magnitude and direction are being studied[61]. Results show destabilization of the plasma slab on the poleward side by a combination of the effects of convection ($\underline{E} \times \underline{B}$) and field aligned currents. Striation-like structures form ~ 1 hour with east-west PSD $\propto k_x^{-n}$, $n \approx 2$-2.5 for 3 km $\lesssim 2\pi/k_x \lesssim 100$ km and north-south PSD $\propto k_y^{-m}$, $m \approx 2$ for 3 km $\lesssim 2\pi/k_y \lesssim 256$ km. In addition, the linear theory of the CCI has been extended[58,59] to include other effects which extend its range of validity. Based on all these results the CCI appears to be a relevant instability mechanism for high latitude scintillation causing irregularity studies. Work is ongoing to extend the instability mechanism to regions other than the diffuse auroral zone. Numerical simulations in the intermediate wavelength (100 m-1km) regime are also under way.

IV. Conclusions

In the present paper, we have exhibited results from the physics modelling of ionospheric irregularity phenomena. We have given results from three F region ionospheric areas: (A) plasma cloud striation phenomena, (B) equatorial spread F phenomena, and (C) high latitude diffuse auroral irregularity phenomena. The irregularities in these three areas can produce deleterious scintillation effects on satellite C^3I systems. The three areas have been studied by deriving the relevant plasma fluid equations with the proper plasma instability mechanisms built in to them

(physics modelling) and then studying these equations using nonlinear numerical simulation techniques. In case (A) the relevant instability mechanism for late time striation phenomena is the $\underline{E} \times \underline{B}$ gradient drift instability mechanism; in (B) it is a form of the collisional Rayleigh-Taylor instability mechanism; and in (C) it is the current convective instability mechanism (or in the case of the two-sided plasma enhancement, a combination of the $\underline{E} \times \underline{B}$ gradient drift instability and current convective instability mechanisms).

The studies presented show that the theoretical and computational programs are at a stage where we can generate detailed information on the causes and structure of ionospheric irregularities. Meaningful information can be obtained on realistic problems. The results provide a basis within which to interpret experimental data and act as a vehicle for suggesting new experiments. The modelling allows us to attain a predictive capability with respect to ionospheric irregularities that can cause C^3I satellite systems scintillation phenomena.

Acknowledgement

This work was supported by the Defense Nuclear Agency and the Office of Naval Research. In addition, we would like to thank our collegues Pradeep Chaturvedi, Joe Huba, and Ed McDonald for their efforts in the study of ionospheric irregularities. Without their accomplishments this article could not have been written.

References

1. Ossakow, S.L., "Ionospheric Irregularities," Rev. Geophys. Space Phys., 17, 521, 1979.
2. Fejer, B.G. and Kelley, M.C., "Ionospheric Irregularities," Rev. Geophys. Space Phys., 18, 401, 1980.
3. Ossakow, S.L., "Spread F Theories-A Review," J. Atm. Terr. Phys., 43, 437, 1981.
4. Kelley, M.C. and McClure, J.P., "Equatorial Spread F: A Review of Recent Experimental Results," J. Atm. Terr. Phys., 43, 427, 1981.
5. Rosenberg, N.W., "Observations of Striation Formation in a Barium Ion Cloud, J. Geophys. Res., 76, 6856, 1971.
6. Davis, T.N., Romick, G.J. Wescott, E.M. Jeffries, R.A., Kerr, D.M., and Peek, H.M., "Observations of the Development of Striations in Large Barium Clouds," Planet. Space Sci., 22, 67, 1974.
7. Baker, K.D., and Ulwick, J.C., "Measurements of Electron Density Structure in Barium Clouds," Geophys. Res. Lett., 5, 723, 1978.
8. Simon, A., "Instability of a Partially Ionized Plasma in Crossed Electric and Magnetic Fields," Phys. Fluids, 6, 382, 1963.
9. Haerendel, G., Lust, R., and Rieger, F., "Motion of Artificial Ion Clouds in the Upper Atmosphere," Planet. Space Sci., 15, 1, 1967.
10. Linson, L.M., and Workman, J.B., "Formation of Striations in Ionospheric Plasma Clouds," J. Geophys. Res., 75, 3211, 1970.
11. Völk, H.J., and Haerendel, G., "Striations in Ionospheric Ion Clouds, 1," J. Geophys. Res., 76, 4541, 1971.
12. Perkins, F.W., Zabusky, N.J., and Doles, J.H. III, "Deformation and Striation of Plasma Clouds in the Ionosphere, 1," J. Geophys. Res., 78, 697, 1973.
13. Chaturvedi, P.K., and Ossakow, S.L., "Nonlinear Stabilization of the E x B Gradient Drift Instability in Ionospheric Plasma Clouds," J. Geophys. Res., 84, 419, 1979.
14. Zabusky, N.J., Doles, J.H. III, and Perkins, F.W., "Deformation and Striation of Plasma Clouds in the Ionosphere, 2, Numerical Simulation of a Nonlinear Two-Dimensional Model," J. Geophys. Res., 78, 711, 1973.

15. Lloyd, J.H., and Haerendel, G., "Numerical Modeling of the Drift and Deformation of Ionospheric Plasma Clouds and of Their Interaction with Other Layers of the Ionosphere," J. Geophys. Res., 78, 7389, 1973.

16. Goldman, S.R., Ossakow, S.L., and Book, D.L., "On the Nonlinear Motion of a Small Barium Cloud in the Ionosphere," J. Geophys. Res., 79, 1471, 1974.

17. Scannapieco, A.J., Ossakow, S.L., Book, D.L., McDonald, B.E., and Goldman, S.R., "Conductivity Ratio Effects on the Drift and Deformation of F Region Barium Clouds Coupled to the E Region Ionosphere," J. Geophys. Res., 79, 2913, 1974.

18. Doles, J.H. III, Zabusky, N.J., and Perkins, F.W., "Deformation and Striation of Plasma Clouds in the Ionosphere, 3, Numerical Simulations of a Multi-level Model with Recombination Chemistry," J. Geophys. Res., 81, 5987, 1976.

19. Ossakow, S.L., Scannapieco, A.J., Goldman, S.R., Book, D.L., and McDonald, B.E., "Theoretical and Numerical Simulation Studies of Ionospheric Inhomogeneities Produced by Plasma Clouds," in Effect of the Ionosphere on Space Systems and Communications, edited by J.M. Goodman, U.S. Government Printing Office, Washington, D.C., 1975.

20. Ossakow, S.L., Zalesak, S.T., and Zabusky, N.J., "Recent Results on Cleavage, Bifurcation, and Cascade Mechanisms in Ionospheric Plasma Clouds," Memo. Rep. 3579, Nav. Res. Lab., Washington, D.C., Aug., 1977.

21. McDonald, B.E., Keskinen, M.J., and Ossakow, S.L., "Computer Simulation of Gradient Drift Instability Processes in Operation Avefria," J. Geophys. Res., 85, 2143, 1980.

22. Scannapieco, A.J., Ossakow, S.L., Goldman, S.R., and Pierre, J.M., "Plasma Cloud Late Time Striation Spectra," J. Geophys. Res., 81, 6037, 1976.

23. McDonald, B.E., Ossakow, S.L., Zalesak, S.T., and Zabusky, N.J., "Determination of Minimum Scale Sizes in Plasma Cloud Striations," in Effect of the Ionosphere on Space and Terrestrial Systems, edited by J.M. Goodman, U.S. Government Printing Office, Washington, D.C., 1978.

24. McDonald, B.E., Ossakow, S.L., Zalesak, S.T., and Zabusky, N.J., "Scale Sizes and Lifetimes of F Region Striations as Determined by the Condition of Marginal Stability," J. Geophys. Res., 86, 5775, 1981.

25. Keskinen, M.J., McDonald, B.E., and Ossakow, S.L., "Preliminary Numerical Study of the Outer Scale Size of Ionospheric Plasma Cloud Striations," J. Geophys. Res., 85, 2349, 1980.

26. Keskinen, M.J., Ossakow, S.L., and Chaturvedi, P.K., "Preliminary Report of Numerical Simulations of Intermediate Wavelength E x B Gradient Drift Instability in Ionospheric Plasma Clouds," J. Geophys. Res., 85, 3485, 1980.

27. Zalesak, S.T., "Fully Multidimensional Flux-corrected Transport Algorithms for Fluids," J. Comp. Phys., 31, 335, 1979.

28. Varga, R.S., Matrix Iterative Analysis, Prentice Hall, Englewood Cliffs, N.J., 1962.

29. McDonald, B.E., "The Chebychev Method for Solving Nonself-Adjoint Elliptic Equations on a Vector Computer," J. Comput. Phys., 35, 147, 1980.

30. Keskinen, M.J. and Ossakow, S.L., "Effect of Different Initial Conditions on the Evolution of the E x B Gradient Drift Instability in Ionospheric Plasma Clouds," Memo Report 4490, Nav. Res. Lab., Washington, D.C., April, 1981.

31. Kelley, M.C., Baker, K.D., and Ulwick, J.C., "Late Time Barium Cloud Striations and Their Possible Relationship to Equatorial Spread F," J. Geophys. Res., 84, 1898, 1979.

32. Keskinen, M.J. and Ossakow, S.L., "On the Spatial Power Spectrum of the E x B Gradient Drift Instability in Ionospheric Plasma Clouds," J. Geophys. Res., 86, 6947, 1981.

33. Booker, H.G. and Wells, H.W., "Scattering of Radio Waves by the F region of the Ionosphere," Terres. Magn., 43, 249, 1938.

34. Kelley, M.C., Haerendel, G., Kappler, H., Valenzuela, A., Balsley, B.B., Carter, D.A., Ecklund, W.L., Carlson, C.W., Hausler, B., and Torbert, R., "Evidence for a Rayleigh-Taylor Type Instability and Upwelling of Depleted Density Regions During Equatorial Spread F," Geophys. Res. Letts., 3, 448, 1976.

35. McClure, J.P., Hanson, W.B., and Hoffman, J.H., "Plasma Bubbles and Irregularities in the Equatorial Ionosphere," J. Geophys. Res., 82, 2650, 1977.

36. Woodman, R.F. and La Hoz, C., "Radar Observations of F Region Equatorial Irregularities," J. Geophys. Res., 81, 5447, 1976.

37. Tsunoda, R.T., "Time Evolution and Dynamics of Equatorial Backscatter Plumes, 1. Growth Phase," J. Geophys. Res., 86, 139, 1981.

38. Scannapieco, A.J., and Ossakow, S.L., "Nonlinear Equatorial Spread F," Geophys. Res. Lett., 3, 451, 1976.

39. Tsunoda, R.T., "On the Spatial Relationship of 1-m Equatorial Spread F Irregularities and Plasma Bubbles," J. Geophys. Res., 85, 185, 1980.

40. Szuszczewicz, E.P., Tsunoda, R.T., Narcisi, R., and Holmes, J.C., "Coincident Radar and Rocket Observations of Equatorial Spread F," Geophys. Res. Lett., 7, 537, 1980.

41. Szuszczewicz, E.P., Tsunoda, R.T., Narcisi, R., and Holmes, J.C., "PLUMEX II: A Second Set of Coincident Radar and Rocket Observations of Equatorial Spread-F," Geophys. Res. Lett., 8, 803, 1981.

42. Ossakow, S.L., Zalesak, S.T., McDonald, B.E., and Chaturvedi, P.K., "Nonlinear Equatorial Spread F: Dependence on Altitude of the F Peak and Bottomside Background Electron Density Gradient Scale Length," J. Geophys. Res., 84, 17, 1979.

43. Zalesak, S.T., and Ossakow, S.L., "Nonlinear Equatorial Spread F: Spatially Large Bubbles Resulting from Large Horizontal Scale Initial Perturbations," J. Geophys. Res., 85, 2131, 1980.

44. Zalesak, S.T., Ossakow, S.L., and Chaturvedi, P.K., "Nonlinear Equatorial Spread F: The Effect of Neutral Winds and Background Pedersen Conductivity," Memo Rept. 4588, Nav. Res. Lab., Washington, D.C., July, 1981.

45. Keskinen, M.J., Ossakow, S.L., and Chaturvedi, P.K., "Preliminary Report of Numerical Simulations of Intermediate Wavelength Collisional Rayleigh-Taylor Instability in Equatorial Spread F," J. Geophys. Res., 85, 1775, 1980.

46. Keskinen, M.J., Szuszczewicz, E.P., Ossakow, S.L., and Holmes, J.C., "Nonlinear Theory and Experimental Observations of the Local Collisional Rayleigh-Taylor Instability in a Descending Equatorial Spread F Ionosphere," J. Geophys. Res., 86, 5785, 1981.

47. Huba, J.D., and Ossakow, S.L., "Diffusion of Small-Scale Density Irregularities During Equatorial Spread F," J. Geophys. Res., 86, 9107, 1981.

48. Kudeki, E., Fejer, B.G., Farley, D.T., and Ierkic, H.M., "Interferometer Studies of Equatorial F Region Irregularities and Drifts," Geophys. Res. Lett., 8, 377, 1981.

49. Tsunoda, R.T., Livingston, R.C., and Rino, C.L., "Evidence of a Velocity Shear in Bulk Plasma Motion Associated with the Post-Sunset Rise of the Equatorial F Layer," Geophys. Res. Lett., 8, 807, 1981.

50. Fremouw, E.J., Rino, C.L., Livingston, R.C., and Cousins, M.C., "A Persistent Subauroral Scintillation Enhancement Observed in Alaska," Geophys. Res. Lett., 4, 539, 1977.

51. Rino, C.L., Livingston, R.C., and Matthews, S.J., "Evidence for Sheet-Like Auroral Ionospheric Irregularities," Geophys. Res. Letts., 5, 1039, 1978.

52. Rino, C.L. and Matthews, S.J., "On the Morphology of Auroral-Zone Radiowave Scintillation," J. Geophys. Res., 85, 4139, 1979.

53. Rino, C.L. and Owen, J., "The Structure of Localized Nighttime Auroral-Zone Scintillation Enhancements," J. Geophys. Res., 85, 2941, 1980.

54. Vickrey, J.F., Rino, C.L., and Potemra, T.A., "Chatanika/Triad Observations of Unstable Ionization Enhancements in the Auroral F-Region," Geophys. Res. Lett., 7, 789, 1980.

55. Ossakow, S.L. and Chaturvedi, P.K., "Current Convective Instability in the Diffuse Aurora," Geophys. Res. Lett., 6, 332, 1979.

56. Kadomtsev, B.B. and Nedospasov, A.V., "Instability of the Positive Column in a Magnetic Field and the Anomalous Diffusion Effect," J. Nucl. Energy, Part C, 1, 230, 1960.

57. Chaturvedi, P.K. and Ossakow, S.L., "Nonlinear Stabilization of the Current Convective Instability in the Diffuse Aurora," Geophys. Res. Lett., 6, 957, 1979.

58. Huba, J.D. and Ossakow, S.L., "Influence of Magnetic Shear on the Current Convective Instability in the Diffuse Aurora," J. Geophys. Res., 85, 6874, 1980.

59. Chaturvedi, P.K. and Ossakow, S.L., "The Current Convective Instability as Applied to the Auroral Ionosphere," J. Geophys. Res., 86, 4811, 1981.

60. Keskinen, M.J., Ossakow, S.L., and McDonald, B.E., "Nonlinear Evolution of Diffuse Auroral F Region Ionospheric Irregularities," Geophys. Res. Lett., 7, 573, 1980.

61. Keskinen, M.J. and Ossakow, S.L., "Nonlinear Evolution of Plasma Enhancements in the Auroral Ionosphere I: Long Wavelength Irregularities," J. Geophys. Res. (in press 1981).

62. Chaturvedi, P.K., "Collisional Ion Cyclotron Waves in the Auroral Ionosphere," J. Geophys. Res., 81, 6169, 1976.

63. Lee, W.W., and Okuda, H., "Anomalous Transport and Stabilization of Collisionless Drift-Wave Instabilities," Phys. Rev. Lett., 36, 870, 1976.

64. Matsuda, Y., and Okuda, H., "Simulation of Dissipative Trapped-Electron Instability in Linear Geometry," Phys. Rev. Lett., 36, 474, 1976.

DISTRIBUTION LIST

DEPARTMENT OF DEFENSE

ASSISTANT SECRETARY OF DEFENSE
COMM, CMD, CONT 7 INTELL
WASHINGTON, D.C. 20301
  01CY ATTN J. BABCOCK
  01CY ATN M. EPSTEIN

DIRECTOR
COMMAND CONTROL TECHNICAL CENTER
PENTAGON RM BF 685
WASHINGTON, D.C. 20301
  01CY ATTN C-650
  01CY ATTN C-312 R. MASON

DIRECTOR
DEFENSE ADVANCED RSCH PROJ AGENCY
ARCHITECT BUILDING
1400 WILSON BLVD.
ARLINGTON, VA. 22209
  01CY ATTN NUCLEAR MONITORING RESEARCH
  01CY ATTN STRATEGIC TECH OFFICE

DEFENSE COMMUNICATION ENGINEER CENTER
1860 WIEHLE AVENUE
RESTON, VA. 22090
  01CY ATTN CODE R820
  01CY ATTN CODE R410 JAMES W. MCLEAN
  01CY ATTN CODE R720 J. WORTHINGTON

DIRECTOR
DEFENSE COMMUNICATIONS AGENCY
WASHINGTON, D.C. 20305
  (ADR CNWDI: ATTN CODE 240 FOR)
  01CY ATTN CODE 101B

DEFENSE TECHNICAL INFORMATION CENTER
CAMERON STATION
ALEXANDRIA, VA. 22314
  (12 COPIES IF OPEN PUBLICATION,
  OTHERWISE 2 COPIES)
  12CY ATTN TC

DIRECTOR
DEFENSE INTELLIGENCE AGENCY
WASHINGTON, D.C. 20301
  01CY ATTN DT-1B
  01CY ATTN DB-4C E. O'FARRELL
  01CY ATTN DIAAP A. WISE
  01CY ATTN DIAST-5
  01CY ATTN DT-1BZ R. MORTON
  01CY ATTN HQ-TR J. STEWART
  01CY ATTN W. WITTIG DC-7D

DIRECTOR
DEFENSE NUCLEAR AGENCY
WASHINGTON, D.C. 20305
  01CY ATTN STVL
  04CY ATTN TITL
  01CY ATTN DDST
  03CY ATTN RAAE

COMMANDER
FIELD COMMAND
DEFENSE NUCLEAR AGENCY
KIRTLAND, AFB, NM 87115
  01CY ATTN FCPR

DIRECTOR
INTERSERVICE NUCLEAR WEAPONS SCHOOL
KIRTLAND AFB, NM 87115
  01CY ATTN DOCUMENT CONTROL

JOINT CHIEFS OF STAFF
WASHINGTON, D.C. 20301
  01CY ATTN J-3 WWMCCS EVALUATION OFFICE

DIRECTOR
JOINT STRAT TGT PLANNING STAFF
OFFUTT AFB
OMAHA, NB 68113
  01CY ATTN JLTW-2
  01CY ATTN JPST G. GOETZ

CHIEF
LIVERMORE DIVISION FLD COMMAND DNA
DEPARTMENT OF DEFENSE
LAWRENCE LIVERMORE LABORATORY
P.O. BOX 808
LIVERMORE, CA 94550
  01CY ATTN FCPRL

DIRECTOR
NATIONAL SECURITY AGENCY
DEPARTMENT OF DEFENSE
FT. GEORGE G. MEADE, MD 20755
  01CY ATTN JOHN SKILLMAN R52
  01CY ATTN FRNK LEONARD
  01CY ATTN W14 PAT CLARK
  01CY ATTN OLIVER H. BARTLETT W32
  01CY ATTN R5

COMMANDANT
NATO SCHOOL (SHAPE)
APO NEW YORK 09172
  01CY ATTN U.S. DOCUMENTS OFFICER

UNDER SECY OF DEF FOR RSCH & ENGRG
DEPARTMENT OF DEFENSE
WASHINGTON, D.C. 20301
01CY ATTN STRATEGIC & SPACE SYSTEMS (OS)

WWMCCS SYSTEM ENGINEERING ORG
WASHINGTON, D.C. 20305
01CY ATTN R. CRAWFORD

COMMANDER/DIRECTOR
ATMOSPHERIC SCIENCES LABORATORY
U.S. ARMY ELECTRONICS COMMAND
WHITE SANDS MISSILE RANGE, NM 88002
01CY ATTN DELAS-EO F. NILES

DIRECTOR
BMD ADVANCED TECH CTR
HUNTSVILLE OFFICE
P.O. BOX 1500
HUNTSVILLE, AL 35807
01CY ATTN ATC-T MELVIN T. CAPPS
01CY ATTN ATC-O W. DAVIES
01CY ATTN ATC-R DON RUSS

PROGRAM MANAGER
BMD PROGRAM OFFICE
5001 EISENHOWER AVENUE
ALEXANDRIA, VA 22333
01CY ATTN DACS-BMT J. SHEA

CHIEF C-E- SERVICES DIVISION
U.S. ARMY COMMUNICATIONS CMD
PENTAGON RM 1B269
WASHINGTON, D.C. 20310
01CY ATTN C- E-SERVICES DIVISION

COMMANDER
FRADCOM TECHNICAL SUPPORT ACTIVITY
DEPARTMENT OF THE ARMY
FORT MONMOUTH, N.J. 07703
01CY ATTN DRSEL-NL-RD H. BENNET
01CY ATTN DRSEL-PL-ENV H. BOMKE
01CY ATTN J.E. QUIGLEY

COMMANDER
HARRY DIAMOND LABORATORIES
DEPARTMENT OF THE ARMY
2800 POWDER MILL ROAD
ADELPHI, MD 20783
(CNWDI-INNER ENVELOPE: ATTN: DELHD-RBH)
01CY ATTN DELHD-TI M. WEINER
01CY ATTN DELHD-RB R. WILLIAMS
01CY ATTN DELHD-NP F. WIMENITZ
01CY ATTN DELHD-NP C. MOAZED

COMMANDER
U.S. ARMY COMM-ELEC ENGRG INSTAL AGY
FT. HUACHUCA, AZ 85613
01CY ATTN CCC-EMEO GEORGE LANE

COMMANDER
U.S. ARMY FOREIGN SCIENCE & TECH CTR
220 7TH STREET, NE
CHARLOTTESVILLE, VA 22901
01CY ATTN DRXST-SD
01CY ATTN R. JONES

COMMANDER
U.S. ARMY MATERIAL DEV & READINESS CMD
5001 EISENHOWER AVENUE
ALEXANDRIA, VA 22333
01CY ATTN DRCLDC J.A. BENDER

COMMANDER
U.S. ARMY NUCLEAR AND CHEMICAL AGENCY
7500 BACKLICK ROAD
BLDG 2073
SPRINGFIELD, VA 22150
01CY ATTN LIBRARY

DIRECTOR
U.S. ARMY BALLISTIC RESEARCH LABORATORY
ABERDEEN PROVING GROUND, MD 21005
01CY ATTN TECH LIBRARY EDWARD BAICY

COMMANDER
U.S. ARMY SATCOM AGENCY
FT. MONMOUTH, NJ 07703
01CY ATTN DOCUMENT CONTROL

COMMANDER
U.S. ARMY MISSILE INTELLIGENCE AGENCY
REDSTONE ARSENAL, AL 35809
01CY ATTN JIM GAMBLE

DIRECTOR
U.S. ARMY TRADOC SYSTEMS ANALYSIS ACTIVITY
WHITE SANDS MISSILE RANGE, NM 88002
01CY ATTN ATAA-SA
01CY ATTN TCC/F. PAYAN JR.
01CY ATTN ATTA-TAC LTC J. HESSE

COMMANDER
NAVAL ELECTRONIC SYSTEMS COMMAND
WASHINGTON, D.C. 20360
01CY ATTN NAVALEX 034 T. HUGHES
01CY ATTN PME 117
01CY ATTN PME 117-T
01CY ATTN CODE 5011

COMMANDING OFFICER
NAVAL INTELLIGENCE SUPPORT CTR
4301 SUITLAND ROAD, BLDG. 5
WASHINGTON, D.C. 20390
  01CY ATTN MR. DUBBIN STIC 12
  01CY ATTN NISC-50
  01CY ATTN CODE 5404 J. GALET

COMMANDER
NAVAL OCCEAN SYSTEMS CENTER
SAN DIEGO, CA 92152
  03CY ATTN CODE 532 W. MOLER
  01CY ATTN CODE 0230 C. BAGGETT
  01CY ATTN CODE 81 R. EASTMAN

DIRECTOR
NAVAL RESEARCH LABORATORY
WASHINGTON, D.C. 20375
  01CY ATTN CODE 4700 TIMOTHY P. COFFEY
        26 CYS IF UNCLASS. 1 CY IF CLASS)
  01CY ATTN CODE 4701 JACK D. BROWN
  01CY ATTN CODE 4780 BRANCH HEAD (150
        CYS IF UNCLASS, 1 CY IF CLASS)
  01CY ATTN CODE 7500
  01CY ATTN CODE 7550
  01CY ATTN CODE 7580
  01CY ATTN CODE 7551
  01CY ATTN CODE 7555
  01CY ATTN CODE 4730 E. MCLEAN
  01CY ATTN CODE 4187

COMMANDER
NAVAL SEA SYSTEMS COMMAND
WASHINGTON, D.C. 20362
  01CY ATTN CAPT R. PITKIN

COMMANDER
NAVAL SPACE SURVEILLANCE SYSTEM
DAHLGREN, VA 22448
  01CY ATTN CAPT J.H. BURTON

OFFICER-IN-CHARGE
NAVAL SURFACE WEAPONS CENTER
WHITE OAK, SILVER SPRING, MD 20910
  01CY ATTN CODE F31

DIRECTOR
STRATEGIC SYSTEMS PROJECT OFFICE
DEPARTMENT OF THE NAVY
WASHINGTON, D.C. 20376
  01CY ATTN NSP-2141
  01CY ATTN NSSP-2722 FRED WIMBERLY

COMMANDER
NAVAL SURFACE WEAPONS CENTER
DAHLGREN LABORATORY
DAHLGREN, VA 22448
  01CY ATTN CODE DF-14 R. BUTLER

OFFICER OF NAVAL RESEARCH
ARLINGTON, VA 22217
  01CY ATTN CODE 465
  01CY ATTN CODE 461
  01CY ATTN CODE 402
  01CY ATTN CODE 420
  01CY ATTN CODE 421

COMMANDER
AEROSPACE DEFENSE COMMAND/DC
DEPARTMENT OF THE AIR FORCE
ENT AFB, CO 80912
  01CY ATTN DC MR. LONG

COMMANDER
AEROSPACE DEFENSE COMMAND/XPD
DEPARTMENT OF THE AIR FORCE
ENT AFB, CO 80912
  01CY ATTN XPDQQ
  01CY ATTN XP

AIR FORCE GEOPHYSICS LABORATORY
HANSCOM AFB, MA 01731
  01CY ATTN OPR HAROLD GARDNER
  01CY ATTN LKB KENNETH S.W. CHAMPION
  01CY ATTN OPR ALVA T. STAIR
  01CY ATTN PHP JULES AARONS
  01CY ATTN PHD JURGEN BUCHAU
  01CY ATTN PHD JOHN P. MULLEN

AF WEAPONS LABORATORY
KIRTLAND AFT, NM 87117
  01CY ATTN SUL
  01CY ATTN CA ARTHUR H. GUENTHER
  01CY ATTN NTYCE 1LT. G. KRAJEI

AFTAC
PATRICK AFB, FL 32925
  01CY ATTN TF/MAJ WILEY
  01CY ATTN TN

AIR FORCE AVIONICS LABORATORY
WRIGHT-PATTERSON AFB, OH 45433
  01CY ATTN AAD WADE HUNT
  01CY ATTN AAD ALLEN JOHNSON

DEPUTY CHIEF OF STAFF
RESEARCH, DEVELOPMENT, & ACQ
DEPARTMENT OF THE AIR FORCE
WASHINGTON, D.C. 20330
 01CY ATTN AFRDQ

HEADQUATERS
ELECTRONIC SYSTEMS DIVISION/XR
DEPARTMENT OF THE AIR FORCE
HANSCOM AFB, MA 01731
 01CY ATTN XR J. DEAS

HEADQUATERS
ELECTRONIC SYSTEMS DIVISION/YSEA
DEPARTMENT OF THE AIR FORCE
HANSCOM AFB, MA 01732
 01CY ATTN YSEA

HEADQUATERS
ELECTRONIC SYSTEMS DIVISION/DC
DEPARTMENT OF THE AIR FORCE
HANSCOM AFB, MA 01731
 01CY ATTN DCKC MAJ J.C. CLARK

COMMANDER
FOREIGN TECHNOLOGY DIVISION, AFSC
WRIGHT-PATTERSON AFB, OH 45433
 01CY ATTN NICD LIBRARY
 01CY ATTN ETDP B. BALLARD

COMMANDER
ROME AIR DEVELOPMENT CENTER, AFSC
GRIFFISS AFB, NY 13441
 01CY ATTN DOC LIBRARY/TSLD
 01CY ATTN OCSE V. COYNE

SAMSO/SZ
POST OFFICE BOX 92960
WORLDWAY POSTAL CENTER
LOS ANGELES, CA 90009
 (SPACE DEFENSE SYSTEMS)
 01CY ATTN SZJ

STRATEGIC AIR COMMAND/XPFS
OFFUTT AFB, NB 68113
 01CY ATTN XPFS MAJ B. STEPHAN
 01CY ATTN ADWATE MAJ BRUCE BAUER
 01CY ATTN NRT
 01CY ATTN DOK CHIEF SCIENTIST

SAMSO/SK
P.O. BOX 92960
WORLDWAY POSTAL CENTER
LOS ANGELES, CA 90009
 01CY ATTN SKA (SPACE COMM SYSTEMS)
 M. CLAVIN

SAMSO/MN
NORTON AFB, CA 92409
(MINUTEMAN)
 01CY ATTN MNNL LTC KENNEDY

COMMANDER
ROME AIR DEVELOPMENT CENTER, AFSC
HANSCOM AFB, MA 01731
 01CY ATTN EEP A. LORENTZEN

DEPARTMENT OF ENERGY
LIBRARY ROOM G-042
WASHINGTON, D.C. 20545
 01CY ATTN DOC CON FOR A. LABOWITZ

DEPARTMENT OF ENERGY
ALBUQUERQUE OPERATIONS OFFICE
P.O. BOX 5400
ALBUQUERQUE, NM 87115
 01CY ATTN DOC CON FOR D. SHERWOOD

EG&G, INC.
LOS ALAMOS DIVISION
P.O. BOX 809
LOS ALAMOS, NM 85544
 01CY ATTN DOC CON FOR J. BREEDLOVE

UNIVERSITY OF CALIFORNIA
LAWRENCE LIVERMORE LABORATORY
P.O. BOX 808
LIVERMORE, CA 94550
 01CY ATTN DOC CON FOR TECH INFO DEPT
 01CY ATTN DOC CON FOR L-389 R. OTT
 01CY ATTN DOC CON FOR L-31 R. HAGER
 01CY ATTN DOC CON FOR L-46 F. SEWARD

LOS ALAMOS SCIENTIFIC LABORATORY
P.O. BOX 1663
LOS ALAMOS, NM 87545
 01CY ATTN DOC CON FOR J. WOLCOTT
 01CY ATTN DOC CON FOR R.F. TASCHEK
 01CY ATTN DOC CON FOR E. JONES
 01CY ATTN DOC CON FOR J. MALIK
 01CY ATTN DOC CON FOR R. JEFFRIES
 01CY ATTN DOC CON FOR J. ZINN
 01CY ATTN DOC CON FOR P. KEATON
 01CY ATTN DOC CON FOR D. WESTERVELT

SANDIA LABORATORIES
P.O. BOX 5800
ALBUQUERQUE, NM 87115
 01CY ATTN DOC CON FOR W. BROWN
 01CY ATTN DOC CON FOR A. THORNBROUGH
 01CY ATTN DOC CON FOR T. WRIGHT
 01CY ATTN DOC CON FOR D. DAHLGREN
 01CY ATTN DOC CON FOR 3141
 01CY ATTN DOC CON FOR SPACE PROJECT DIV

SANDIA LABORATORIES
LIVERMORE LABORATORY
P.O. BOX 969
LIVERMORE, CA 94550
  01CY ATTN DOC CON FOR B. MURPHEY
  01CY ATTN DOC CON FOR T. COOK

OFFICE OF MILITARY APPLICATION
DEPARTMENT OF ENERGY
WASHINGTON, D.C. 20545
  01CY ATTN DOC CON DR. YO SONG

<u>OTHER GOVERNMENT</u>

CENTRAL INTELLIGENCE AGENCY
ATTN RD/SI, RM 5G48, HQ BLDG
WASHINGTON, D.C. 20505
  01CY ATTN OSI/PSID RM 5F 19

DEPARTMENT OF COMMERCE
NATIONAL BUREAU OF STANDARDS
WASHINGTON, D.C. 20234
  (ALL CORRES: ATTN SEC OFFICER FOR)
  01CY ATTN R. MOORE

INSTITUTE FOR TELECOM SCIENCES
NATIONAL TELECOMMUNICATIONS & INFO ADMIN
BOULDER, CO 80303
  01CY ATTN A. JEAN (UNCLASS ONLY)
  01CY ATTN W. UTLAUT
  01CY ATTN D. CROMBIE
  01CY ATTN L. BERRY

NATIONAL OCEANIC & ATMOSPHERIC ADMIN
ENVIRONMENTAL RESEARCH LABORATORIES
DEPARTMENT OF COMMERCE
BOULDER, CO 80302
  01CY ATTN R. GRUBB
  01CY ATTN AERONOMY LAB G. REID

<u>DEPARTMENT OF DEFENSE CONTRACTORS</u>

AEROSPACE CORPORATION
P.O. BOX 92957
LOS ANGELES, CA 90009
  01CY ATTN I. GARFUNKEL
  01CY ATTN T. SALMI
  01CY ATTN V. JOSEPHSON
  01CY ATTN S. BOWER
  01CY ATTN N. STOCKWELL
  01CY ATTN D. OLSEN

ANALYTICAL SYSTEMS ENGINEERING CORP
5 OLD CONCORD ROAD
BURLINGTON, MA 01803
  01CY ATTN RADIO SCIENCES

BERKELEY RESEARCH ASSOCIATES, INC.
P.O. BOX 983
BERKELEY, CA 94701
  01CY ATTN J. WORKMAN
  01CY ATTN C. PRETTIE

BOEING COMPANY, THE
P.O. BOX 3707
SEATTLE, WA 98124
  01CY ATTN G. KEISTER
  01CY ATTN D. MURRAY
  01CY ATTN G. HALL
  01CY ATTN J. KENNEY

BROWN ENGINEERING COMPANY, INC.
CUMMINGS RESEARCH PARK
HUNTSVILLE, AL 35807
  01CY ATTN ROMEO A. DELIBERIS

CALIFORNIA AT SAN DIEGO, UNIV OF
P.O. BOX 6049
SAN DIEGO, CA 92106

CHARLES STARK DRAPER LABORATORY, INC.
555 TECHNOLOGY SQUARE
CAMBRIDGE, MA 02139
  01CY ATTN D.B. COX
  01CY ATTN J.P. GILMORE

COMSAT LABORATORIES
LINTHICUM ROAD
CLARKSBURG, MD 20734
  01CY ATTN G. HYDE

CORNELL UNIVERSITY
DEPARTMENT OF ELECTRICAL ENGINEERING
ITHACA, NY 14850
  01CY ATTN D.T. FARLEY, JR.

ELECTROSPACE SYSTEMS, INC.
BOX 1359
RICHARDSON, TX 75080
  01CY ATTN H. LOGSTON
  01CY ATTN SECURITY (PAUL PHILLIPS)

ESL, INC.
495 JAVA DRIVE
SUNNYVALE, CA 94086
  01CY ATTN J. ROBERTS
  01CY ATTN JAMES MARSHALL

GENERAL ELECTRIC COMPANY
SPACE DIVISION
VALLEY FORGE SPACE CENTER
GODDARD BLVD KING OF PRUSSIA
P.O. BOX 8555
PHILADELPHIA, PA 19101
01CY ATTN M.H. BORTNER SPACE SCI LAB

GENERAL ELECTRIC COMPANY
P.O. BOX 1122
SYRACUSE, NY 13201
01CY ATTN F. REIBERT

GENERAL ELECTRIC TECH SERVICES CO., INC.
HMES
COURT STREET
SYRACUSE, NY 13201
01CY ATTN G. MILLMAN

GENERAL RESEARCH CORPORATION
SANTA BARBARA DIVISION
P.O. BOX 6770
SANTA BARBARA, CA 93111
01CY ATTN JOHN ISE, JR.
01CY ATTN JOEL GARBARINO

GEOPHYSICAL INSTITUTE
UNIVERSITY OF ALASKA
FAIRBANKS, AK 99701
(ALL CLASS ATTN: SECURITY OFFICER)
01CY ATTN T.N. DAVIS (UNCLASS ONLY)
01CY ATTN TECHNICAL LIBRARY
01CY ATTN NEAL BROWN (UNCLASS ONLY)

GTE SYLVANIA, INC.
ELECTRONICS SYSTEMS GRP-EASTERN DIV
77 A STREET
NEEDHAM, MA 02194
01CY ATTN MARSHALL CROSS

HSS, INC.
2 ALFRED CIRCLE
BEDFORD, MA 01730
01CY ATTN DONALD HANSEN

ILLINOIS, UNIVERSITY OF
107 COBLE HALL
150 DAVENPORT HOUSE
CHAMPAIGN, IL 61820
(ALL CORRES ATTN DAN MCCLELLAND)
01CY ATTN K. YEH

INSTITUTE FOR DEFENSE ANALYSES
400 ARMY-NAVY DRIVE
ARLINGTON, VA 22202
01CY ATTN J.M. AEIN
01CY ATTN ERNEST BAUER
01CY ATTN HANS WOLFARD
01CY ATTN JOEL BENGSTON

INTL TEL & TELEGRAPH CORPORATION
500 WASHINGTON AVENUE
NUTLEY, NJ 07110
01CY ATTN TECHNICAL LIBRARY

JAYCOR
11011 TORREYANA ROAD
P.O. BOX 85154
SAN DIEGO, CA 92138
01CY ATTN J.L. SPERLING

JOHNS HOPKINS UNIVERSITY
APPLIED PHYSICS LABORATORY
JOHNS HOPKINS ROAD
LAURAL, MD 20810
01CY ATTN DOCUMENT LIBRARIAN
01CY ATTN THOMAS POTEMRA
01CY ATTN JOHN DASSOULAS

KAMAN SCIENCES CORP
P.O. BOX 7463
COLORADO SPRINGS, CO 80933
01CY ATTN T. MEAGHER

KAMAN TEMPO-CENTER FOR ADVANCED STUDIES
816 STATE STREET (P.O DRAWER QQ)
SANTA BARBARA, CA 93102
01CY ATTN DASIAC
01CY ATTN TIM STEPHANS
01CY ATTN WARREN S. KNAPP
01CY ATTN WILLIAM MCNAMARA
01CY ATTN B. GAMBILL

LINKABIT CORP
10453 ROSELLE
SAN DIEGO, CA 92121
01CY ATTN IRWIN JACOBS

LOCKHEED MISSILES & SPACE CO., INC
P.O. BOX 504
SUNNYVALE, CA 94088
01CY ATTN DEPT 60-12
01CY ATTN D.R. CHURCHILL

LOCKHEED MISSILES & SPACE CO., INC.
3251 HANOVER STREET
PALO ALTO, CA 94304
01CY ATTN MARTIN WALT DEPT 52-12
01CY ATTN W.L. IMHOF DEPT 52-12
01CY ATTN RICHARD G. JOHNSON DEPT 52-12
01CY ATTN J.B. CLADIS DEPT 52-12

LOCKHEED MISSILE & SPACE CO., INC.
HUNTSVILLE RESEARCH & ENGR. CTR.
4800 BRADFORD DRIVE
HUNTSVILLE, AL 35807
ATTN DALE H. DIVIS

MARTIN MARIETTA CORP
ORLANDO DIVISION
P.O. BOX 5837
ORLANDO, FL 32805
01CY ATTN R. HEFFNER

M.I.T. LINCOLN LABORATORY
P.O. BOX 73
LEXINGTON, MA 02173
01CY ATTN DAVID M. TOWLE
01CY ATTN P. WALDRON
01CY ATTN L. LOUGHLIN
01CY ATTN D. CLARK

MCDONNEL DOUGLAS CORPORATION
5301 BOLSA AVENUE
HUNTINGTON BEACH, CA 92647
01CY ATTN N. HARRIS
01CY ATTN J. MOULE
01CY ATTN GEORGE MROZ
01CY ATTN W. OLSON
01CY ATTN R.W. HALPRIN
01CY ATTN TECHNICAL LIBRARY SERVICES

MISSION RESEARCH CORPORATION
735 STATE STREET
SANTA BARBARA, CA 93101
01CY ATTN P. FISCHER
01CY ATTN W.F. CREVIER
01CY ATTN STEVEN L. GUTSCHE
01CY ATTN D. SAPPENFIELD
01CY ATTN R. BOGUSCH
01CY ATTN R. HENDRICK
01CY ATTN RALPH KILB
01CY ATTN DAVE SOWLE
01CY ATTN F. FAJEN
01CY ATTN M. SCHEIBE
01CY ATTN CONRAD L. LONGMIRE
01CY ATTN WARREN A. SCHLUETER

MITRE CORPORATION, THE
P.O. BOX 208
BEDFORD, MA 01730
01CY ATTN JOHN MORGANSTERN
01CY ATTN G. HARDING
01CY ATTN C.E. CALLAHAN

MITRE CORP
WESTGATE RESEARCH PARK
1820 DOLLY MADISON BLVD
MCLEAN, VA 22101
01CY ATTN W. HALL
01CY ATTN W. FOSTER

PACIFIC-SIERRA RESEARCH CORP
1456 CLOVERFIELD BLVD.
SANTA MONICA, CA 90404
01CY ATTN E.C. FIELD, JR.

PENNSYLVANIA STATE UNIVERSITY
IONOSPHERE RESEARCH LAB
318 ELECTRICAL ENGINEERING EAST
UNIVERSITY PARK, PA 16802
(NO CLASS TO THIS ADDRESS)
01CY ATTN IONOSPHERIC RESEARCH LAB

PHOTOMETRICS, INC.
442 MARRETT ROAD
LEXINGTON, MA 02173
01CY ATTN IRVING L. KOFSKY

PHYSICAL DYNAMICS, INC.
P.O. BOX 3027
BELLEVUE, WA 98009
01CY ATTN E.J. FREMOUW

PHYSICAL DYNAMICS, INC.
P.O. BOX 10367
OAKLAND, CA 94610
ATTN A. THOMSON

R & D ASSOCIATES
P.O. BOX 9695
MARINA DEL REY, CA 90291
01CY ATTN FORREST GILMORE
01CY ATTN BRYAN GABBARD
01CY ATTN WILLIAM B. WRIGHT, JR.
01CY ATTN ROBERT F. LELEVIER
01CY ATTN WILLIAM J. KARZAS
01CY ATTN H. ORY
01CY ATTN C. MACDONALD
01CY ATTN R. TURCO

RAND CORPORATION, THE
1700 MAIN STREET
SANTA MONICA, CA 90406
01CY ATTN CULLEN CRAIN
01CY ATTN ED BEDROZIAN

RAYTHEON CO.
528 BOSTON POST ROAD
SUDBURY, MA 01776
01CY ATTN BARBARA ADAMS

RIVERSIDE RESEARCH INSTITUTE
80 WEST END AVENUE
NEW YORK, NY 10023
01CY ATTN VINCE TRAPANI

SCIENCE APPLICATIONS, INC.
P.O. BOX 2351
LA JOLLA, CA 92038
01CY ATTN LEWIS M. LINSON
01CY ATTN DANIEL A. HAMLIN
01CY ATTN E. FRIEMAN
01CY ATTN E.A. STRAKER
01CY ATTN CURTIS A. SMITH
01CY ATTN JACK MCDOUGALL

SCIENCE APPLICATIONS, INC
1710 GOODRIDGE DR.
MCLEAN, VA 22102
ATTN: J. COCKAYNE

SRI INTERNATIONAL
333 RAVENSWOOD AVENUE
MENLO PARK, CA 94025
01CY ATTN DONALD NEILSON
01CY ATTN ALAN BURNS
01CY ATTN G. SMITH
01CY ATTN L.L. COBB
01CY ATTN DAVID A. JOHNSON
01CY ATTN WALTER G. CHESNUT
01CY ATTN CHARLES L. RINO
01CY ATTN WALTER JAYE
01CY ATTN M. BARON
01CY ATTN RAY L. LEADABRAND
01CY ATTN G. CARPENTER
01CY ATTN G. PRICE
01CY ATTN J. PETERSON
01CY ATTN R. HAKE, JR.
01CY ATTN V. GONZALES
01CY ATTN D. MCDANIEL

STEWART RADIANCE LABORATORY
UTAH STATE UNIVERSITY
1 DE ANGELO DRIVE
BEDFORD, MA 01730
01CY ATTN J. ULWICK

TECHNOLOGY INTERNATIONAL CORP
75 WIGGINS AVENUE
BEDFORD, MA 01730
01CY ATTN W.P. BOQUIST

TRW DEFENSE & SPACE SYS GROUP
ONE SPACE PARK
REDONDO BEACH, CA 90278
01CY ATTN R. K. PLEBUCH
01CY ATTN S. ALTSCHULER
01CY ATTN D. DEE

VISIDYNE
SOUTH BEDFORD STREET
BURLINGTON, MASS 01803
01CY ATTN W. REIDY
01CY ATTN J. CARPENTER
01CY ATTN C. HUMPHREY

Code 2623 - 20 Copies

IONOSPHERIC MODELING DISTRIBUTION LIST
(UNCLASSIFIED ONLY)

PLEASE DISTRIBUTE ONE COPY TO EACH OF THE FOLLOWING PEOPLE:

NAVAL RESEARCH LABORATORY
WASHINGTON, D.C. 20375
DR. P. MANGE - CODE 4101
DR. R. MEIER - CODE 4141
DR. E. SZUSZCZEWICZ - CODE 4187
DR. J. GOODMAN - CODE 4180
Dr. R. RODRIGUEZ - CODE 4187

A.F. GEOPHYSICS LABORATORY
L.G. HANSCOM FIELD
BEDFORD, MA 01730
DR. T. ELKINS
DR. W. SWIDER
MRS. R. SAGALYN
DR. J.M. FORBES
DR. T.J. KENESHEA
DR. J. AARONS
DR. H. CARLSON
DR. J. JASPERSE

CORNELL UNIVERSITY
ITHACA, NY 14850
DR. W.E. SWARTZ
DR. R. SUDAN
DR. D. FARLEY
DR. M. KELLEY

HARVARD UNIVERSITY
HARVARD SQUARE
CAMBRIDGE, MA 02138
DR. M.B. McELROY
DR. R. LINDZEN

INSTITUTE FOR DEFENSE ANALYSIS
400 ARMY/NAVY DRIVE
ARLINGTON, VA 22202
DR. E. BAUER

MASSACHUSETTS INSTITUTE OF TECHNOLOGY
PLASMA FUSION CENTER
LIBRARY, NW16-262
CAMBRIDGE, MA 02139

NASA
GODDARD SPACE FLIGHT CENTER
GREENBELT, MD 20771
DR. S. CHANDRA
DR. K. MAEDA
DR. R.F. BENSON

NATIONAL TECHNICAL INFORMATION CENTER
CAMERON STATION
ALEXANDRIA, VA 22314
12CY ATTN TC

COMMANDER
NAVAL AIR SYSTEMS COMMAND
DEPARTMENT OF THE NAVY
WASHINGTON, D.C. 20360
DR. T. CZUBA

COMMANDER
NAVAL OCEAN SYSTEMS CENTER
SAN DIEGO, CA 92152
MR. R. ROSE - CODE 5321

NOAA
DIRECTOR OF SPACE AND ENVIRONMENTAL LABORATORY
BOULDER, CO 80302
DR. A. GLENN JEAN
DR. G.W. ADAMS
DR. D.N. ANDERSON
DR. K. DAVIES
DR. R. F. DONNELLY

OFFICE OF NAVAL RESEARCH
800 NORTH QUINCY STREET
ARLINGTON, VA 22217
DR. H. MULLANEY

PENNSYLVANIA STATE UNIVERSITY
UNIVERSITY PARK, PA 16802
DR. J.S. NISBET
DR. P.R. ROHRBAUGH
DR. L.A. CARPENTER
DR. M. LEE
DR. R. DIVANY
DR. P. BENNETT
DR. E. KLEVANS

PRINCETON UNIVERSITY
PLASMA PHYSICS LABORATORY
PRINCETON, NJ 08540
DR. F. PERKINS

SCIENCE APPLICATIONS, INC.
1150 PROSPECT PLAZA
LA JOLLA, CA 92037
DR. D.A. HAMLIN
DR. L. LINSON
DR. E. FRIEMAN

STANFORD UNIVERSITY
STANFORD, CA 94305
DR. P.M. BANKS

U.S. ARMY ABERDEEN RESEARCH
AND DEVELOPMENT CENTER
BALLISTIC RESEARCH LABORATORY
ABERDEEN, MD
DR. J. HEIMERL

UNIVERSITY OF CALIFORNIA,
BERKELEY
BERKELEY, CA 94720
DR. M. HUDSON

UNIVERSITY OF CALIFORNIA
LOS ALAMOS SCIENTIFIC LABORATORY
J-10, MS-664
LOS ALAMOS, NM 87545
M. PONGRATZ
D. SIMONS
G. BARASCH
L. DUNCAN
P. BERNHARDT

UNIVERSITY OF CALIFORNIA,
LOS ANGELES
405 HILLGARD AVENUE
LOS ANGELES, CA 90024
DR. F.V. CORONITI
DR. C. KENNEL
DR. A.Y. WONG

UNIVERSITY OF MARYLAND
COLLEGE PARK, MD 20740
DR. K. PAPADOPOULOS
DR. E. OTT

UNIVERSITY OF PITTSBURGH
PITTSBURGH, PA 15213
DR. N. ZABUSKY
DR. M. BIONDI
DR. E. OVERMAN

UTAH STATE UNIVERSITY
4TH AND 8TH STREETS
LOGAN, UTAH 84322
DR. R. HARRIS
DR. K. BAKER
DR. R. SCHUNK

FILMED

3-8